Order Number 1345437

Capacitance calculations for 3D VLSI interconnection geometries

Omer, Ahmed Adan, M.S.

The University of Arizona, 1991

U·M·I
300 N. Zeeb Rd.
Ann Arbor, MI 48106

CAPACITANCE CALCULATIONS FOR 3D VLSI INTERCONNECTION GEOMETRIES

by

Ahmed Adan Omer

A Thesis Submitted to the Faculty of the

DEPARTMENT OF THE ELECTRICAL AND COMPUTER ENGINEERING

In Partial Fulfillment of the Requirements
For the Degree of

MASTER OF SCIENCE

WITH A MAJOR IN ELECTRICAL ENGINEERING

In the Graduate College

THE UNIVERSITY OF ARIZONA

1 9 9 1

STATEMENT BY AUTHOR

This thesis has been submitted in partial fulfillment of requirements for an advanced degree at The University of Arizona and is deposited in the University Library to be made available to borrowers under rules of the Library.

Brief quotations from this thesis are allowable without special permission, provided that accurate acknowledgment of source is made. Requests for permission for extended quotation from or reproduction of this manuscript in whole or in part may be granted by the head of the major department or the Dean of the Graduate College when in his or her judgement the proposed use of the material is in the interests of scholarship. In all other instances, however, permission must be obtained from the author.

SIGNED: 

APPROVAL BY THESIS DIRECTOR

This thesis has been approved on the date shown below:

A.C. Cangellaris

Assistant Professor of Electrical Engineering

6/30/91

Date

ACKNOWLEDGEMENTS

First and foremost I would like to thank my advisor Dr. Andreas Cangellaris for his contributions to this work as well as for his guidance and encouragement. I am grateful to Dr. Cangellaris for having confidence in me and being supportive at all times. Special thanks to Dr. Steve Dvorak for all the help he has provided including reviewing this thesis and following it through to its completion. I also wish to thank Dr. Olgierd Palusinski for reviewing this thesis and providing many helpful suggestions.

This research was made possible by the financial support of the Semiconductor Research Corporation. I would like to extend my appreciation to Dr. John L. Prince for his help in obtaining this support.

Many thanks go to Dr. Donald G. Dudley and Dr. James R. Wait for their support both in and out of the classroom during my studies at Arizona. In addition, I would like to thank the many past and present members of the Electromagnetics Laboratory who helped in numerous ways with this research; in particular, M. Chan, Dr. R. Lee, J. Judkins, M. Gribbons, M. Mechaik, M. Pasik, C. Spring, and D. Wright. I would also like to thank Dr. Richard W. Ziolkowski for keeping me company late at night in the Lab and providing helpful insights to my questions.

Yet this list would be incomplete should I fail to mention my officemates, C. Abernethy, C. Baumgartner, W. Mi, and L. Vakanas, and the members of the Electronic Packaging Laboratory who responded promptly whenever I seek their help.

Lastly, I would like to thank my family for their support and patience with my educational career.

CONTENTS

TABLE OF CONTENTS – continued

LIST OF ILLUSTRATIONS

LIST OF ILLUSTRATIONS – continued

ABSTRACT

An integral equation formulation for the calculation of the capacitance of three-dimensional VLSI geometries is presented. A proper combination of 2D and 3D methods is used for efficient numerical computations. The method of moments is used for the solution of the integral equation. In addition, Green's functions that satisfy the boundary conditions at the dielectric interfaces are implemented in order to minimize the number of unknowns involved in the numerical solution. The mathematical formulation presented here and the associated computer program are appropriate for obtaining the capacitance matrix of complex three-dimensional multi-conductor configurations of the microstrip and the stripline type. Finally, numerical results for the per-unit- length capacitance and total capacitance of several intercoinnections are provided and compared with known results. Applications include the extraction of lumped capacitive elements used in the equivalent circuit representations of coupled conductor bends, vias and crossovers. In addition, calculations of per-unit-length capacitance of coupled flaring lines are performed.

CHAPTER 1

INTRODUCTION

Packaging of VLSI electronic circuits is the science and art of establishing *interconnections* and a suitable operating environment for electronic circuits to process or store information. Electronic packages contain many— in the case of computers many millions— electronic circuit components, including, resistors, capacitors, diodes, and transistors. To form circuits, these components need to be interconnected. Individual circuit blocks must also be connected with each other to form functional units.

With such interconnections, three electrical parameters— resistance, capacitance, and inductance— are always present and cause signal delays and many forms of signal distortion, including the unwanted appearance of signals on supposedly quiescent lines. It is these unwanted noise signals that cause the biggest problems. Since they are hard to eliminate from a finished design, they must be addressed during the initial design phase.

Proper packaging design (geometries and materials) can be used to control the signal line capacitance to the reference plane, the line resistance, its self-inductance, and the interline capacitances and inductances. Consequently, good designs minimize signal distortion, and the appearance of unwanted interference [Tumala and Rymaszewski, 1989].

Actually, the resistance may be neglected in some cases, since conductors used in VLSI interconnections are highly conductive. In addition, in most cases,

the materials used in packaging are non-magnetic; therefore, the inductances can be calculated from the capacitances as we shall show later.

As the switching of logic gates becomes faster, the coupling effect between densely spaced interconnections plays an ever increasing role in the timing analysis of the whole system. The capacitance between these sometimes complicated interconnections then becomes a crucial element in the modeling and computer-aided electrical analysis of high-perfomance systems [Wu, 1988].

From a computer-aided analysis point of view, interconnection structures are modeled as a network of multiple, coupled transmission lines. Once the per-unit-length (p.u.l.) capacitance and inductance matrices for each section of the multicondutor transmission line (MTL) network are found, the transmission line equations are implemented to analyze the transient behavior of the interconnections. For an N-conductor MTL embedded in a homogeneous dielectric, there are N distinct dominant transverse electric and magnetic (TEM) modes that can independently propagate along its axis. Since the TEM waves do not have any longitudinal field components, the field distribution in the transverse plane is the same as in the static case and the analysis can be carried out using static potentials. On the other hand, for an N-conductor MTL embedded in an inhomogeneous dielectric media, there are N distinct dominant hybrid electric and magnetic (HEM) modes which can propagate along its axis and have zero cutoff frequencies analogous to the TEM modes. However, at low frequencies the longitudinal components of the fields are negligibly small and the dominant HEM modes become almost TEM or quasi-TEM; therefore, they are analyzed as such.

Moreover, considering each MTL section as a set of parallel conductors supporting quasi-TEM fields along its axis, it will be assumed that discontinuities occur at the junctions between two or more sections. Examples of such discontinuities include bends, stubs, and vias. Under certain conditions that will be discussed later, the electromagnetic characterization of such discontinuities leads to an equivalent circuit representation of lumped capacitances and inductances that allows us to model the effect of the discontinuities on the fundamental quasi-TEM mode of propagation [Cangellaris et al, 1990].

In the last two decades, a large amount of work has been devoted to the calculation of capacitance and inductance matrices for MTL embedded in a multilayered dielectric medium. However, the majority of the work has been of a two-dimensional (2-D) type, where the assumption is made that the conductors are infinitely long and of invariant cross-section along the direction of propagation. Even though the 2-D methods save both computer storage and time, they are useless when the MTL conductors contain discontinuities or their cross-section varies along the direction of propagation. For such cases, a three-dimensional (3-D) analysis is necessary. In this work, capacitance calculations are made for general interconnection geometries using proper combinations of 2-D and 3-D approaches. For finite-length conductors and at the vicinity of discontinuities, 3-D analysis is employed. However, those parts of the MTL structure that extend uniformly to infinity and are distant from discontinuities are treated using 2-D methods.

Several methods have been proposed to deal with the capacitance calculations for 3-D multiconductor systems including the finite element method (FEM) and the integral equation method (IEM). Both methods employ a large number of

unknowns to approximate, for FEM, the potential distribution in the space surrounding the conductors or, for IEM, the charge distribution on the conductor surfaces. The FEM is advantageous when the interconnect geometry is very complex or media is highly inhomogeneous. However, for most practical packaging structures, the environment is homogeneous or at most has a layered inhomogeneity. In such cases, the IEM is much more efficient [Wu and Wu, 1988]. This is the approach taken in this work.

In Chapter 2, the specific problem of interest is described. Also, the TEM approximation and its validity for multiconductor multidielectric waveguides is discussed. Because we calculate the capacitance from the charges on the conductor surfaces, the relations between these two quantities is discussed. Starting from the electrostatic equations, we define the boundary value problem that is to solved. As a matter of fact, the boundary value problem turns out to be Laplace's equation with Dirichlet boundrary conditions. Next, an integral equation is formulated that can be solved for the unknown surface charge densities. Finally, the Green's functions associated with the specific geometry are presented.

The solution of the integral equation is discussed in Chapter 3. The method of moments is used to reduce the integral equation into a system of linear equations. The solution procedure for both the 2-D and 3-D problems are described in this chapter. In addition, the procedure used to discretize the conductor surfaces is explained. Discussion on the numerical evaluation of the integrals involved is also included. In order to determine number of discrete elements for efficient capacitance calculation, a study of this sort is given at the end of this chapter.

Capacitance calculations of several structures are given in Chapter 4. The capacitance of a simple rectangular conductor box is given. Other applications include the computation of the excess capacitances of a cross-over stripline, a via, single and coupled bends, and per-unit-lenght capacitances of single and coupled flaring lines.

CHAPTER 2

PROBLEM STATEMENT AND MATHEMATICAL FORMULATION

Our aim in this chapter is to formally define the problem of interest. That is, to describe the physical geometry, explain the underlying approximations and assumptions, state the boundary-value problem, and formulate an appropriate integral equation that can be used for its solution. Along the way, we will discuss how transmission line theory can be applied to interconnection systems under the quasi-TEM propagation assumption, and thus justify the need for obtaining the capacitance matrices associated with the interconnect conductor geometry. Also, we will discuss how the capacitances can be computed from the charge distribution on conductors, which in turn can be obtained from the solution of Laplace's equation with Dirichlet boundary conditions on the surfaces of the conductors. Finally, the formulation of the integral equation and the associated Green's functions will be described.

2.1 The TEM Approximation

A waveguide system consisting of conductors embedded in an inhomogeneous medium supports only hybrid modes. However, at sufficiently low frequencies the propagating hybrid modes have small longitudinal field components relative to the transverse fields [Carin and Webb, 1989]. By low frequencies we mean frequencies such that the corresponding wavelength in the dielectric medium is large compared to the cross-sectional dimensions of the multiconductor system. Under

this condition, the hybrid modes look almost like TEM modes; therefore, they are commonly called quasi-TEM modes.

Actually, for multi-conductor, multi-dielectric interconnections with perfect conductors of constant cross section along the direction of energy propagation, the TEM approximation has been shown to be valid for slowly varying signals and lines with small transverse inhomogeneity [Lindell and Gu, 1987]. Since the longitudinal field components are assumed negligible in the TEM approximation, the generalized transmission-line theory is usually used for simulation of signal propagation on such systems.

For a lossless system, the transmission line parameters are found in terms of per-unit-length (p.u.l.) capacitance and inductance matrices. To calculate the p.u.l. capacitance matrix an electrostatic problem is solved. Furthermore, if the media are non-magnetic, it is not necessary to solve the magnetostatic problem to calculate the p.u.l. inductance matrix. Instead, the p.u.l. capacitance matrix $[C_H]$ for the specific conductor geometry embedded in a homogeneous dielectric medium ϵ is calculated first and then the inductance matrix $[L]$ is found as [Wei et al, 1984]

$$[L] = (\mu_0 \epsilon)[C_H]^{-1}. \tag{2.1}$$

In addition, at sufficiently low frequencies, discontinuities are modeled by equivalent lumped capacitive and inductive elements. In this work, we will also consider the computation of these capacitive elements for single and coupled discontinuities. Figure 2–1 provides examples of the type of conductor configurations that will be considered in this work. As a matter of fact, these are representative of interconnections used in VLSI electronic packages.

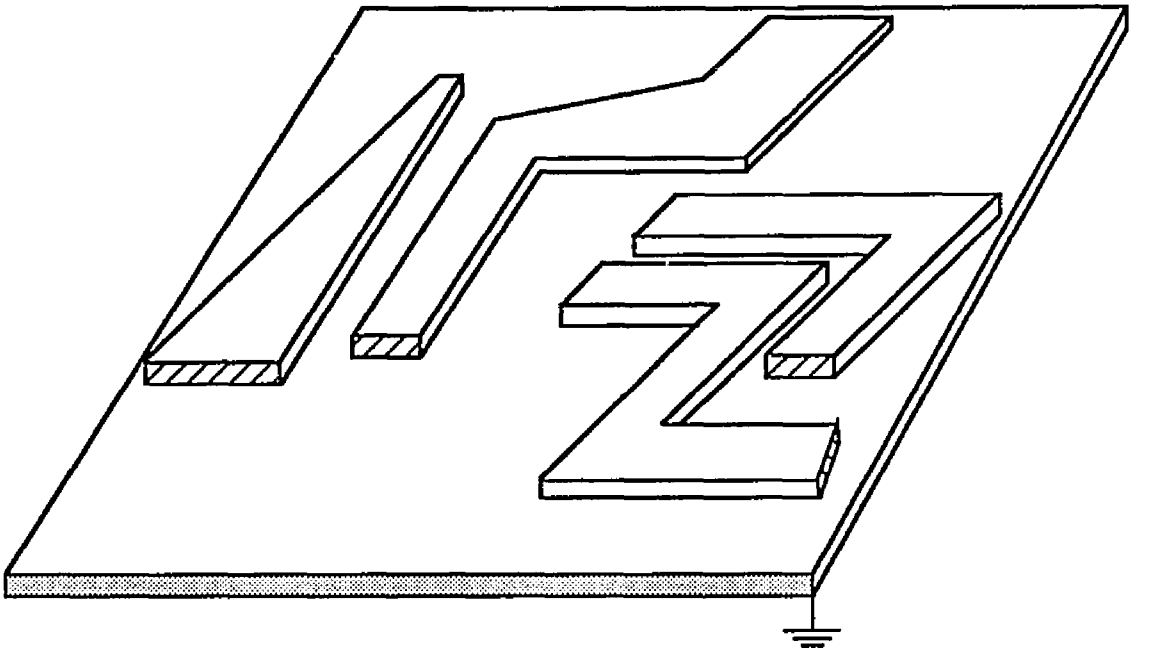

Figure 2-1 Examples of three-dimensional packaging interconnections.

A typical cross section of the geometries under consideration is shown in Figure 2–2. An arbitrary number of finite-length and infinitely-long conductors are embedded in a two-layer dielectric medium above a perfectly conducting ground plane of infinite extent located at $y = 0$. The dielectric interface is parallel to the ground plane and separates the dielectric layer of thickness h and permittivity ϵ_2 from the homogeneous dielectric region of permittivity ϵ_1 extending to infinity in the $+y$ direction. The conductor sides can be of arbitrary planar shapes; however, any conductor cross-section perpendicular to the xz plane will be assumed to be rectangular.

We shall assume that the conductors have infinite conductivity. Thus, the charge will accumulate on the surface of the conductors and the electric field will be zero inside the conductors. Also, the potential on any given conductor will be constant in the transverse plane.

2.2 Capacitance and Charge Relations

With the perfect ground as reference, let V_j be the constant electrostatic potential on the jth conductor. The total charge on the ith conductor is then

$$\sum_{j=1}^{N_C} C_{ij} V_j = Q_i, \quad i = 1, 2, \ldots, N_C \tag{2.2}$$

where N_C is the total number of conductors, C_{ij}, $i \neq j$, is the mutual capacitance between the ith and jth conductors, and C_{ii} is the self capacitance of the ith conductor. Letting $V_k = 1$ and $V_j = 0$ for $j \neq k$, (2.2) becomes

$$C_{ik} = Q_i^{(k)}, \quad i = 1, 2, \ldots, N_C \tag{2.3}$$

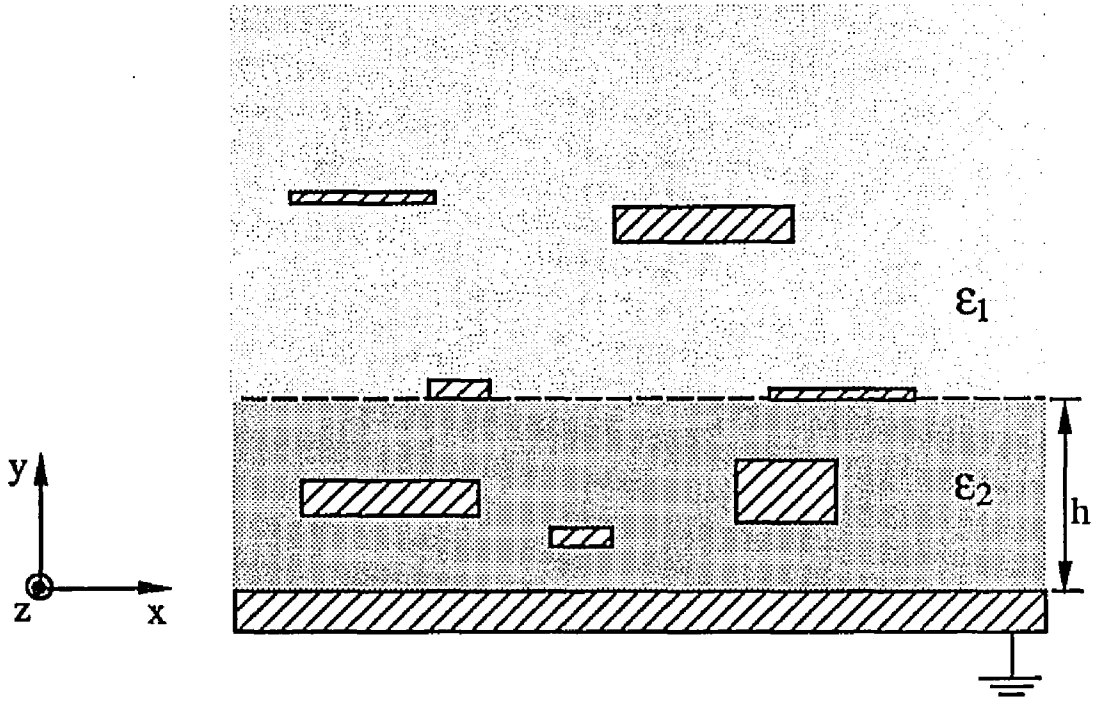

Figure 2-2 Cross section of a typical packaging geometry.

where the superscript (k) is used to indicate that all conductors except conductor k are grounded. This last equation indicates that the self and mutual capacitances can be obtained in terms of the induced charges on the conductors calculated from the solution of N_C electrostatic boundary-value problems, where the boundary conditions for the kth problem are $V_k = 1$, and $V_j = 0$ for $j \neq k$.

For the case of a multiconductor waveguiding structure, the desirable quantity is the p.u.l. capacitance matrix of the structure. With the assumption of a smoothly varying cross section of the multi-conductor system along the direction of propagation, the p.u.l. capacitance matrix can be obtained in the following manner. Let L be the length of the interconnection structure along its axis of propagation w. Equation (2.3) can be written as

$$C_{ik} = Q_i^{(k)} = \int_0^L q_i^{(k)}(w)dw, \quad i = 1, 2, \ldots, N_C \tag{2.4}$$

where $q_i^{(k)}(w)$ is the per-unit-length charge on the ith conductor with boundary conditions $V_k = 1$ and $V_j = 0$, $j \neq k$. This last equation suggests that the elements of the p.u.l. capacitance matrix of the interconnection structure are given by

$$c_{ik}(w) = q_i^{(k)}(w), \quad i = 1, 2, \ldots, N_C, \quad k = 1, 2, \ldots, N_C \tag{2.5}$$

For the kth boundary value problem with boundary conditions $V_k = 1$, $V_j = 0$, $j \neq k$, an integral equation will be solved for the unknown charge distributions on the surfaces of the conductors. But first we need to discuss how to obtain this integral equation for the specific conductor/dielectric geometry.

2.3 The Electrostatic Case and Laplace's Equation

For the electrostatic case, two of Maxwell's equation are employed:

$$\nabla \times \mathbf{E}(\mathbf{r}) = 0 \tag{2.6}$$

$$\nabla \cdot \mathbf{D}(\mathbf{r}) = \rho(\mathbf{r}) \tag{2.7}$$

where $\mathbf{E}$ is the electric field, $\mathbf{D}$ is the electric displacement, and ρ is the charge density at point $\mathbf{r}$. Equation (2.6) suggests that the electric field must be the gradient of a scalar potential. Thus,

$$\mathbf{E}(\mathbf{r}) = -\nabla\phi(\mathbf{r}) \tag{2.8}$$

where $\phi(\mathbf{r})$ is the electric potential. The negative sign is chosen according to the traditional convention. Since a linear, isotropic media is assumed, $\mathbf{D}(\mathbf{r}) = \epsilon(\mathbf{r})\mathbf{E}(\mathbf{r})$, and we can rewrite (2.7) as

$$-\nabla \cdot (\epsilon(\mathbf{r})\mathbf{E}(\mathbf{r})) = \rho(\mathbf{r}). \tag{2.9}$$

Noting that there are not any imposed free charges ($\rho = 0$) and combining (2.8) and (2.9) we obtain

$$\nabla \cdot (\epsilon(\mathbf{r})\nabla\phi(\mathbf{r})) = 0 \tag{2.10}$$

which is Laplace's equation for the electrical potential. However, for the specific two-layer geometry, $\epsilon(\mathbf{r})$ suffers a jump at the dielectric interface. Furthermore, each layer is homogeneous. Thus, the appropriate statement of (2.10) is

$$\epsilon_n \nabla^2 \phi(\mathbf{r}) = 0 \tag{2.11}$$

where

$$\epsilon_n = \begin{cases} \epsilon_1, & y > h; \\ \epsilon_2, & 0 < y < h. \end{cases}$$

Assuming that an electic charge distribution of finite extent exists in a 3-D region ofspace, (2.11) is subject to the following boundary conditions :

$$\phi(\mathbf{r})\Big|_{y=h^+} = \phi(\mathbf{r})\Big|_{y=h^-} \tag{2.12a}$$

$$\epsilon_1 \frac{\partial \phi}{\partial y}\Big|_{y=h^+} = \epsilon_2 \frac{\partial \phi}{\partial y}\Big|_{y=h^-} \tag{2.12b}$$

$$\phi(\mathbf{r})\Big|_{y=0} = 0 \tag{2.13a}$$

$$\lim_{\mathbf{r}\to\infty} \phi(\mathbf{r}) = 0 \tag{2.13b}$$

For the given boundary value problem defined, our task is to formulate an integral equation which can be solved for the unknown charge density on the conductor surfaces.

2.4 The Integral Equation

In order to solve the nonhomogeneous partial differential equation (2.11) subject to boundary conditions (2.12) and (2.13), we introduce the Green's function $G(\mathbf{r}, \mathbf{r}')$ for Poisson's equation:

$$\nabla \cdot \left(\epsilon(\mathbf{r}) \nabla G(\mathbf{r}, \mathbf{r}')\right) = -\delta(\mathbf{r} - \mathbf{r}') \tag{2.14}$$

subject to the same boundary conditions as $\phi(\mathbf{r})$ in (2.12) and (2.13). Here, $\mathbf{r}$ and $\mathbf{r}'$ are position vectors for a field point and a source point, respectively. In fact, in what follows, we shall use the convention that the primed coordinates refer to the

source, while the unprimed coordinates are used to refer to the field. Using Green's second identity for ϕ and G [Haberman, 1987]

$$\int_{V^{(1)}} \left(\phi \nabla^2 G - G \nabla^2 \phi\right) dv = \oint_{S^{(1)}} \left(\phi \frac{\partial G}{\partial n} - G \frac{\partial \phi}{\partial n}\right) ds \tag{2.15a}$$

$$\int_{V^{(2)}} \left(\phi \nabla^2 G - G \nabla^2 \phi\right) dv = \oint_{S^{(2)}} \left(\phi \frac{\partial G}{\partial n} - G \frac{\partial \phi}{\partial n}\right) ds \tag{2.15b}$$

where $\hat{\mathbf{n}}$ is the outward pointing normal vector, $V^{(1)}$ is the volume bounded by the dielectric interface ($y = h$) and the surface at infinity ($\mathbf{r} \to \infty$), and $S^{(1)}$ is the surface boundary of $V^{(1)}$ as shown in Figure 2–3. Similarly, $V^{(2)}$ is the volume of the region between the dielectric interface and the ground plane $y = 0$ and the surface at infinity (i.e. $x \to \pm\infty$ and $z \to \pm\infty$), and $S^{(2)}$ is the bounding surface of $V^{(2)}$. We define $S^{(1)} = S_D^{(1)} + S_C^{(1)} + S_h^+$ and $S^{(2)} = S_D^{(2)} + S_C^{(2)} + S_h^-$, where $S_C^{(1)}$ and $S_C^{(2)}$ are the conductor surfaces in regions 1 and 2, respectively, and $S_h^{\pm}$ is the surface at $y = h^{\pm}$. Then (2.15a,b) become

$$\int_{V^{(1)}} \left(\phi \nabla^2 G - G \nabla^2 \phi\right) dv = \int_{S_D^{(1)}} \left(\phi \frac{\partial G}{\partial n} - G \frac{\partial \phi}{\partial n}\right) ds + \int_{S_C^{(1)}} \left(\phi \frac{\partial G}{\partial n} - G \frac{\partial \phi}{\partial n}\right) ds + \int_{S_h^+} \left(\phi \frac{\partial G}{\partial n} - G \frac{\partial \phi}{\partial n}\right) ds \tag{2.16a}$$

$$\int_{V^{(2)}} \left(\phi \nabla^2 G - G \nabla^2 \phi\right) dv = \int_{S_D^{(2)}} \left(\phi \frac{\partial G}{\partial n} - G \frac{\partial \phi}{\partial n}\right) ds + \int_{S_C^{(2)}} \left(\phi \frac{\partial G}{\partial n} - G \frac{\partial \phi}{\partial n}\right) ds + \int_{S_h^-} \left(\phi \frac{\partial G}{\partial n} - G \frac{\partial \phi}{\partial n}\right) ds \tag{2.16b}$$

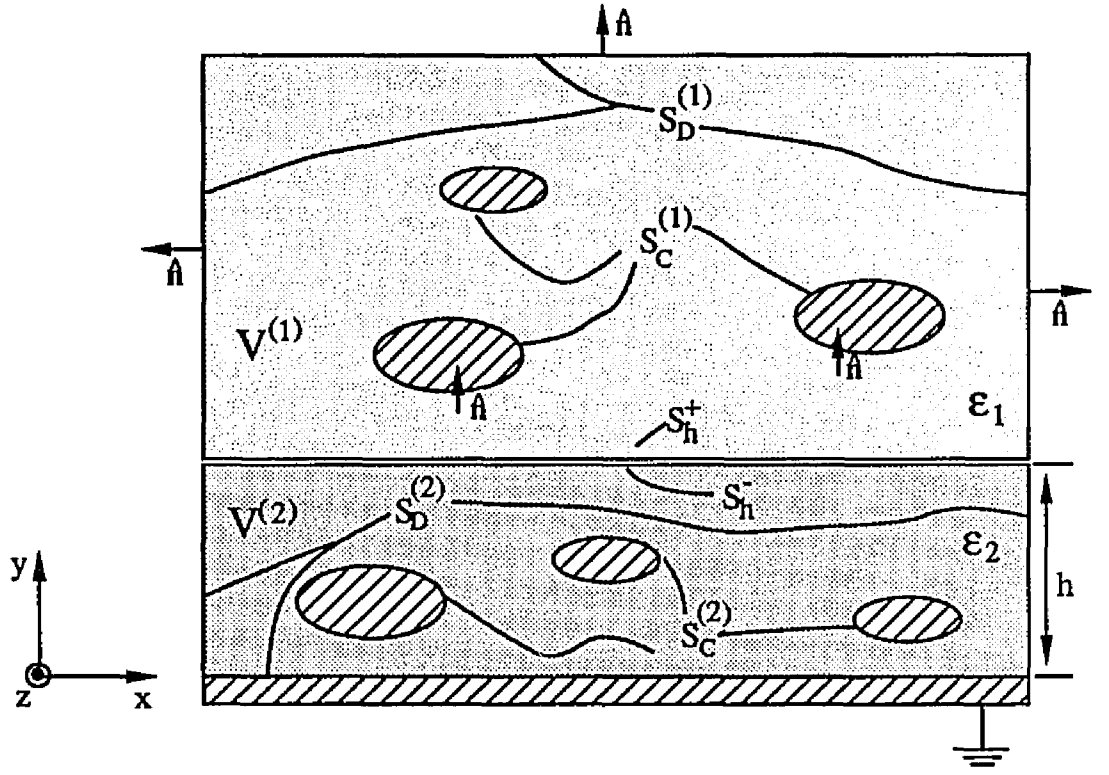

Figure 2-3 Cross section of the geometry showing the various regions and their surface boundaries.

According to the boundary conditions in (2.13), the surface integrals on $S_D^{(1)}$ and $S_D^{(2)}$ vanish. Thus,

$$\int_{V^{(1)}} \left(\phi\nabla^2 G - G\nabla^2\phi\right) dv = \int_{S_C^{(1)}} \left(\phi\frac{\partial G}{\partial n} - G\frac{\partial \phi}{\partial n}\right) ds + \int_{S_h^+} \left(\phi\frac{\partial G}{\partial n} - G\frac{\partial \phi}{\partial n}\right) ds \tag{2.17a}$$

$$\int_{V^{(2)}} \left(\phi\nabla^2 G - G\nabla^2\phi\right) dv = \int_{S_C^{(2)}} \left(\phi\frac{\partial G}{\partial n} - G\frac{\partial \phi}{\partial n}\right) ds + \int_{S_h^-} \left(\phi\frac{\partial G}{\partial n} - G\frac{\partial \phi}{\partial n}\right) ds \tag{2.17b}$$

Adding (2.17a) and (2.17b) and noting that

$$\epsilon_2 \int_{S_h^-} \left(\phi\frac{\partial G}{\partial n} - G\frac{\partial \phi}{\partial n}\right) ds = -\epsilon_1 \int_{S_h^+} \left(\phi\frac{\partial G}{\partial n} - G\frac{\partial \phi}{\partial n}\right) ds \tag{2.18}$$

we obtain

$$\epsilon_1 \int_{V^{(1)}} \left(\phi\nabla^2 G - G\nabla^2\phi\right) dv + \epsilon_2 \int_{V^{(2)}} \left(\phi\nabla^2 G - G\nabla^2\phi\right) dv = \epsilon_1 \int_{S_C^{(1)}} \left(\phi\frac{\partial G}{\partial n} - G\frac{\partial \phi}{\partial n}\right) ds + \epsilon_2 \int_{S_C^{(2)}} \left(\phi\frac{\partial G}{\partial n} - G\frac{\partial \phi}{\partial n}\right) ds \tag{2.19}$$

Substituting (2.11) and (2.14) into (2.19), and rearranging the equation, we obtain

$$-\int_V \phi\delta(\mathbf{r} - \mathbf{r}')dv = \int_{S_C} \epsilon\phi\frac{\partial G}{\partial n}ds - \int_{S_C} \epsilon G\frac{\partial \phi}{\partial n}ds \tag{2.20}$$

where $V = V^{(1)} + V^{(2)}$ and $S_C = S_C^{(1)} + S_C^{(2)}$. Assume N_C conductors are present. Recognizing the surface charge density , $\sigma = \epsilon\frac{\partial \phi}{\partial n}$, and the fact that the potential

on the conductors is constant, e.g. on the ith conductor $\phi(\mathbf{r}) = \phi_i$, (2.20) becomes

$$\phi(\mathbf{r}') = -\sum_{i=1}^{N_C} \phi_i \left(\oint_{S_i} \epsilon \frac{\partial G}{\partial n} ds \right) + \sum_{i=1}^{N_C} \left(\oint_{S_i} \sigma_i G ds \right) \tag{2.21}$$

where S_i is the surface of the ith conductor and σ_i the surface charge distribution on that conductor. The integral $\oint_{S_i} \epsilon \frac{\partial G}{\partial n} ds$ represents the electric flux through the closed surface S_i due to an exterior charge. By Gauss' law, it is identically zero. Hence,

$$\phi(\mathbf{r}') = \sum_{i=1}^{N_C} \left(\oint_{S_i} \sigma_i(\mathbf{r}) G(\mathbf{r}, \mathbf{r}') ds \right). \tag{2.22}$$

In view of the reciprocal character of $G(\mathbf{r}, \mathbf{r}')$, we can interchange $\mathbf{r}$ and $\mathbf{r}'$.

$$\phi(\mathbf{r}) = \sum_{i=1}^{N_C} \left(\oint_{S_i} \sigma_i(\mathbf{r}') G(\mathbf{r}, \mathbf{r}') ds' \right). \tag{2.23}$$

In general, the conductors can be infinitely long or of finite length. Without loss of generality, let us consider the case of N_C infinitely long conductors possessing local discontinuities like bends or vias. We wish to use a 3-D analysis at the vicinity of the discontinuities, and a 2-D analysis for the remaining of the conductor surfaces that extend to infinity. For this reason, (2.23) can be split into three integrals

$$\phi(\mathbf{r}) = I^{-\infty}(\mathbf{r}) + I^{3d}(\mathbf{r}) + I^{+\infty}(\mathbf{r}) \tag{2.24a}$$

where

$$I^{-\infty}(\mathbf{r}) = \sum_{i=1}^{N_C} \sum_{j=1}^{N_{S_i}} \left(\int_{W_{ij}} \hat{\sigma}_{ij}(\mathbf{r}') G^{-\infty}(\mathbf{r}, \mathbf{r}') d\ell' \right) \tag{2.24b}$$

$$I^{3d}(\mathbf{r}) = \sum_{i=1}^{N_C} \sum_{j=1}^{N_{S_i}} \left(\int_{W_{ij}} \sigma_{ij}(\mathbf{r}') G^{3d}(\mathbf{r}, \mathbf{r}') d\ell' \right) \tag{2.24c}$$

$$I^{+\infty}(\mathbf{r}) = \sum_{i=1}^{N_C} \sum_{j=1}^{N_{S_i}} \left(\int_{W_{ij}} \hat{\sigma}_{ij}(\mathbf{r}') G^{+\infty}(\mathbf{r}, \mathbf{r}') d\ell' \right) \tag{2.24d}$$

Here, G^{3d} is the potential due to a unit line charge of finite length. $G^{-\infty}$ and $G^{+\infty}$ are potentials due to semi-infinitely long unit line charges extending to $-\infty$ and $+\infty$, respectively. $\hat{\sigma}_{ij}$ is the surface charge density obtained from the 2-D problem. In addition, the conductor sides are dealt as separate surfaces as is apparent from the introduction of the second summation. N_{S_i} is the number of sides of the ith conductor, and σ_{ij}, W_{ij} represent the surface charge density and the surface of the jth side of the ith conductor, respectively. If we make the approximation that at distances sufficiently far from the discontinuties the charge distribution is mainly that of an infinitely long conductor of the same cross section, $\hat{\sigma}_{ij}$ can be found from the solution of the 2-D problem. The following equation is used to form the integral equation for the 2-D case

$$\phi(\mathbf{r}) = \sum_{i=1}^{N_C} \sum_{j=1}^{N_{S_i}} \left(\int_{W_{ij}} \hat{\sigma}_{ij}(\mathbf{r}') G^{2d}(\mathbf{r}, \mathbf{r}') d\ell' \right). \tag{2.25}$$

where G^{2d} is the potential due to an infinitely long line of unit charge.

For the kth boundary value problem, when the potential is evaluated for points on the conductor surfaces ($\mathbf{r} = \mathbf{r}_s$) one has

$$\phi(\mathbf{r}_s) = V_l = \begin{cases} 1, & \text{if } l = k \\ 0, & \text{if } l \neq k \end{cases} \tag{2.26}$$

Therefore, the integral equation for the 2-D problem is

$$\sum_{i=1}^{N_C}\sum_{j=1}^{N_{S_i}}\left(\int_{W_{ij}}\hat{\sigma}_{ij}(\mathbf{r}')G^{2d}(\mathbf{r}_s,\mathbf{r}')d\ell'\right)=V_l \qquad l=1,\cdots,N_C. \tag{2.27}$$

Likewise, the equation for the 3-D case is

$$\sum_{i=1}^{N_C}\sum_{j=1}^{N_{S_i}}\left(\int_{W_{ij}}\sigma_{ij}(\mathbf{r}')G^{3d}(\mathbf{r}_s,\mathbf{r}')ds'\right)=V_l-I^{-\infty}(\mathbf{r}_s)-I^{+\infty}(\mathbf{r}_s) \qquad l=1,\cdots,N_C. \tag{2.28}$$

The above two equations form the required integral equations for the solution of the boundry value problem described by (2.11), (2.12), and (2.13). In order to solve these equations the method of moments will be implemented in the next chapter. The Green's functions used in these integral equations are presented next.

2.5 Green's Functions

The derivation of the Green's functions used in the above equations is given in Appendix A. There are four sets of these functions: a set for a finite length line, two sets for semi-infinitely long lines, one extending to $-\infty$ and the other to $+\infty$, and one set for an infinitely long line that extends from $-\infty$ to $+\infty$. Actually, the Green's function for the infinitely long line is the Green's function for the 2-D problem. Each of these sets includes four expressions for the four different source/observation point locations. We will use two subscripts to identify each of these functions. The first subscipt refers to the source point and the second

subscript refers to the field point. Subscript a means above the interface, while b stands for below the interface.

For all these Green's functions $\Delta z_1 = z_1 - z$, $\Delta z_2 = z_2 - z$, $\Delta x = x - x'$, and $\Delta y = y - y'$. We define z_1 to be the left endpoint of a line source, while z_2 is the right endpoint on the z axis.

2.5.1 Finite-length line source

The following is the Green's function for a unit line source that extends from z_1 to z_2.

$$G^{3d}(x,y,z;x',y',z_1,z_2) = \begin{cases} G^{3d}_{aa}(x,y,z;x',y',z_1,z_2), & y' \geq h,\ y \geq h \\ G^{3d}_{ab}(x,y,z;x',y',z_1,z_2), & y' \geq h,\ y < h \\ G^{3d}_{ba}(x,y,z;x',y',z_1,z_2), & y' < h,\ y \geq h \\ G^{3d}_{bb}(x,y,z;x',y',z_1,z_2), & y' < h,\ y < h \end{cases} \tag{2.29}$$

$$\begin{aligned} G^{3d}_{aa} = \frac{1}{4\pi\epsilon_1}\Bigg[& \ln\left(\frac{\Delta z_2 + \sqrt{\Delta z_2{}^2 + \Delta x^2 + \Delta y^2}}{\Delta z_1 + \sqrt{\Delta z_1{}^2 + \Delta x^2 + \Delta y^2}} \frac{\Delta z_1 + \sqrt{\Delta z_1{}^2 + \Delta x^2 + (y+y')^2}}{\Delta z_2 + \sqrt{\Delta z_2{}^2 + \Delta x^2 + (y+y')^2}}\right) \\ & + \sum_{k=1}^{\infty} \left(\frac{\epsilon_1 - \epsilon_2}{\epsilon_1 + \epsilon_2}\right)^k \ln\Bigg(\frac{\Delta z_2 + \sqrt{\Delta z_2{}^2 + \Delta x^2 + (y+y'+2(k-2)h)^2}}{\Delta z_1 + \sqrt{\Delta z_1{}^2 + \Delta x^2 + (y+y'+2(k-2)h)^2}} \\ & \times \frac{\Delta z_1 + \sqrt{\Delta z_1{}^2 + \Delta x^2 + (y+y'+2kh)^2}}{\Delta z_2 + \sqrt{\Delta z_2{}^2 + \Delta x^2 + (y+y'+2kh)^2}}\Bigg)\Bigg] \end{aligned} \tag{2.30}$$

$$G_{ab}^{3d} = \frac{1}{2\pi(\epsilon_1+\epsilon_2)} \sum_{k=0}^{\infty} \left[\left(\frac{\epsilon_1-\epsilon_2}{\epsilon_1+\epsilon_2} \right)^k \ln \left\{ \frac{\Delta z_2 + \sqrt{{\Delta z_2}^2 + \Delta x^2 + (y-y'-2kh)^2}}{\Delta z_1 + \sqrt{{\Delta z_1}^2 + \Delta x^2 + (y-y'-2kh)^2}} \right.\right.$$

$$\left.\left. \times \frac{\Delta z_1 + \sqrt{{\Delta z_1}^2 + \Delta x^2 + (y+y'+2kh)^2}}{\Delta z_2 + \sqrt{{\Delta z_2}^2 + \Delta x^2 + (y+y'+2kh)^2}} \right\} \right] \tag{2.31}$$

$$G_{ba}^{3d} = \frac{1}{2\pi(\epsilon_1+\epsilon_2)} \sum_{k=0}^{\infty} \left[\left(\frac{\epsilon_1-\epsilon_2}{\epsilon_1+\epsilon_2} \right)^k \ln \left\{ \frac{\Delta z_2 + \sqrt{{\Delta z_2}^2 + \Delta x^2 + (y-y'+2kh)^2}}{\Delta z_1 + \sqrt{{\Delta z_1}^2 + \Delta x^2 + (y-y'+2kh)^2}} \right.\right.$$

$$\left.\left. \times \frac{\Delta z_1 + \sqrt{{\Delta z_1}^2 + \Delta x^2 + (y+y'+2kh)^2}}{\Delta z_2 + \sqrt{{\Delta z_2}^2 + \Delta x^2 + (y+y'+2kh)^2}} \right\} \right] \tag{2.32}$$

$$G_{bb}^{3d} = \frac{1}{4\pi\epsilon_2}\Bigg[\ln\Bigg\{\frac{\Delta z_2 + \sqrt{\Delta z_2{}^2 + \Delta x^2 + \Delta y^2}}{\Delta z_1 + \sqrt{\Delta z_1{}^2 + \Delta x^2 + \Delta y^2}}\frac{\Delta z_1 + \sqrt{\Delta z_1{}^2 + \Delta x^2 + (y+y')^2}}{\Delta z_2 + \sqrt{\Delta z_2{}^2 + \Delta x^2 + (y+y')^2}}\Bigg\}$$

$$+\sum_{k=1}^{\infty}\left(\frac{\epsilon_1-\epsilon_2}{\epsilon_1+\epsilon_2}\right)^k \ln\Bigg\{\frac{\Delta z_2 + \sqrt{\Delta z_2{}^2 + \Delta x^2 + (y-y'+2kh)^2}}{\Delta z_1 + \sqrt{\Delta z_1{}^2 + \Delta x^2 + (y-y'+2kh)^2}}$$

$$\times\frac{\Delta z_1 + \sqrt{\Delta z_1{}^2 + \Delta x^2 + (y+y'+2kh)^2}}{\Delta z_2 + \sqrt{\Delta z_2{}^2 + \Delta x^2 + (y+y'+2kh)^2}}$$

$$\times\frac{\Delta z_2 + \sqrt{\Delta z_2{}^2 + \Delta x^2 + (y-y'-2kh)^2}}{\Delta z_1 + \sqrt{\Delta z_1{}^2 + \Delta x^2 + (y-y'-2kh)^2}}$$

$$\times\frac{\Delta z_1 + \sqrt{\Delta z_1{}^2 + \Delta x^2 + (y+y'-2kh)^2}}{\Delta z_2 + \sqrt{\Delta z_2{}^2 + \Delta x^2 + (y+y'-2kh)^2}}\Bigg\}\Bigg] \tag{2.33}$$

2.5.2 Semi-infinite line source extending to $-\infty$

The following is the Green's function for a unit line source that extends from $-\infty$ to z_2.

$$G^{-\infty}(x,y,z;x',y',z_2) = \begin{cases} G_{aa}^{-\infty}(x,y,z;x',y',z_2), & y' \geq h,\ y \geq h \\ G_{ab}^{-\infty}(x,y,z;x',y',z_2), & y' \geq h,\ y < h \\ G_{ba}^{-\infty}(x,y,z;x',y',z_2), & y' < h,\ y \geq h \\ G_{bb}^{-\infty}(x,y,z;x',y',z_2), & y' < h,\ y < h \end{cases} \tag{2.34}$$

$$G_{aa}^{-\infty} = \frac{1}{4\pi\epsilon_1}\left[\ln\frac{-\Delta z_2 + \sqrt{\Delta z_2{}^2 + \Delta x^2 + (y+y')^2}}{-\Delta z_2 + \sqrt{\Delta z_2{}^2 + \Delta x^2 + \Delta y^2}}\right.$$

$$\left. + \sum_{k=1}^{\infty}\left(\frac{\epsilon_1 - \epsilon_2}{\epsilon_1 + \epsilon_2}\right)^k \ln\frac{-\Delta z_2 + \sqrt{\Delta z_2{}^2 + \Delta x^2 + (y+y'+2kh)^2}}{-\Delta z_2 + \sqrt{\Delta z_2{}^2 + \Delta x^2 + (y+y'+2(k-2)h)^2}}\right] \tag{2.35}$$

$$G_{ab}^{-\infty} = \frac{1}{2\pi(\epsilon_1+\epsilon_2)}\sum_{k=0}^{\infty}\left[\left(\frac{\epsilon_1 - \epsilon_2}{\epsilon_1 + \epsilon_2}\right)^k \ln\frac{-\Delta z_2 + \sqrt{\Delta z_2{}^2 + \Delta x^2 + (y+y'+2kh)^2}}{-\Delta z_2 + \sqrt{\Delta z_2{}^2 + \Delta x^2 + (y-y'-2kh)^2}}\right] \tag{2.36}$$

$$G_{ba}^{-\infty} = \frac{1}{2\pi(\epsilon_1+\epsilon_2)}\sum_{k=0}^{\infty}\left[\left(\frac{\epsilon_1 - \epsilon_2}{\epsilon_1 + \epsilon_2}\right)^k \ln\frac{-\Delta z_2 + \sqrt{\Delta z_2{}^2 + \Delta x^2 + (y+y'+2kh)^2}}{-\Delta z_2 + \sqrt{\Delta z_2{}^2 + \Delta x^2 + (y-y'+2kh)^2}}\right] \tag{2.37}$$

$$G_{bb}^{-\infty} = \frac{1}{4\pi\epsilon_2}\left[\ln\frac{-\Delta z_2 + \sqrt{\Delta z_2{}^2 + \Delta x^2 + (y+y')^2}}{-\Delta z_2 + \sqrt{\Delta z_2{}^2 + \Delta x^2 + \Delta y^2}}\right.$$

$$+ \sum_{k=1}^{\infty}\left(\frac{\epsilon_1 - \epsilon_2}{\epsilon_1 + \epsilon_2}\right)^k \ln\left\{\frac{-\Delta z_2 + \sqrt{\Delta z_2{}^2 + \Delta x^2 + (y+y'+2kh)^2}}{-\Delta z_2 + \sqrt{\Delta z_2{}^2 + \Delta x^2 + (y-y'+2kh)^2}}\right.$$

$$\left.\left. \times \frac{-\Delta z_2 + \sqrt{\Delta z_2{}^2 + \Delta x^2 + (y+y'-2kh)^2}}{-\Delta z_2 + \sqrt{\Delta z_2{}^2 + \Delta x^2 + (y-y'-2kh)^2}}\right\}\right] \tag{2.38}$$

2.5.3 Semi-infinite line source extending to $+\infty$

The following is the Green's function for a unit line source that extends from z_1 to $+\infty$.

$$G^{+\infty}(x,y,z;x',y',z_1) = \begin{cases} G_{aa}^{+\infty}(x,y,z;x',y',z_1), & y' \geq h,\ y \geq h \\ G_{ab}^{+\infty}(x,y,z;x',y',z_1), & y' \geq h,\ y < h \\ G_{ba}^{+\infty}(x,y,z;x',y',z_1), & y' < h,\ y \geq h \\ G_{bb}^{+\infty}(x,y,z;x',y',z_1), & y' < h,\ y < h \end{cases} \tag{2.39}$$

$$G_{aa}^{+\infty} = \frac{1}{4\pi\epsilon_1}\left[\ln\frac{\Delta z_1 + \sqrt{{\Delta z_1}^2 + \Delta x^2 + (y+y')^2}}{\Delta z_1 + \sqrt{{\Delta z_1}^2 + \Delta x^2 + \Delta y^2}} + \sum_{k=1}^{\infty}\left(\frac{\epsilon_1-\epsilon_2}{\epsilon_1+\epsilon_2}\right)^k \ln\frac{\Delta z_1 + \sqrt{{\Delta z_1}^2 + \Delta x^2 + (y+y'+2kh)^2}}{\Delta z_1 + \sqrt{{\Delta z_1}^2 + \Delta x^2 + (y+y'+2(k-2)h)^2}}\right] \tag{2.40}$$

$$G_{ab}^{+\infty} = \frac{1}{2\pi(\epsilon_1+\epsilon_2)}\sum_{k=0}^{\infty}\left[\left(\frac{\epsilon_1-\epsilon_2}{\epsilon_1+\epsilon_2}\right)^k \ln\frac{\Delta z_1 + \sqrt{{\Delta z_1}^2 + \Delta x^2 + (y+y'+2kh)^2}}{\Delta z_1 + \sqrt{{\Delta z_1}^2 + \Delta x^2 + (y-y'-2kh)^2}}\right] \tag{2.41}$$

$$G_{ba}^{+\infty} = \frac{1}{2\pi(\epsilon_1+\epsilon_2)}\sum_{k=0}^{\infty}\left[\left(\frac{\epsilon_1-\epsilon_2}{\epsilon_1+\epsilon_2}\right)^k \ln\frac{\Delta z_1 + \sqrt{{\Delta z_1}^2 + \Delta x^2 + (y+y'+2kh)^2}}{\Delta z_1 + \sqrt{{\Delta z_1}^2 + \Delta x^2 + (y-y'+2kh)^2}}\right] \tag{2.42}$$

$$G_{bb}^{+\infty} = \frac{1}{4\pi\epsilon_2}\Bigg[\ln\frac{\Delta z_1 + \sqrt{\Delta z_1{}^2 + \Delta x^2 + (y+y')^2}}{\Delta z_1 + \sqrt{\Delta z_1{}^2 + \Delta x^2 + \Delta y^2}} + \sum_{k=1}^{\infty}\left(\frac{\epsilon_1-\epsilon_2}{\epsilon_1+\epsilon_2}\right)^k \ln\Bigg\{\frac{\Delta z_1 + \sqrt{\Delta z_1{}^2 + \Delta x^2 + (y+y'+2kh)^2}}{\Delta z_1 + \sqrt{\Delta z_1{}^2 + \Delta x^2 + (y-y'+2kh)^2}} \times \frac{\Delta z_1 + \sqrt{\Delta z_1{}^2 + \Delta x^2 + (y+y'-2kh)^2}}{\Delta z_1 + \sqrt{\Delta z_1{}^2 + \Delta x^2 + (y-y'-2kh)^2}}\Bigg\}\Bigg] \tag{2.43}$$

2.5.4 Infinite line source

The following is the Green's function for a unit line source that extends from $-\infty$ to $+\infty$.

$$G^{2d}(x,y;x',y') = \begin{cases} G_{aa}^{2d}(x,y;x',y'), & y' \geq h,\ y \geq h \\ G_{ab}^{2d}(x,y;x',y'), & y' \geq h,\ y < h \\ G_{ba}^{2d}(x,y;x',y'), & y' < h,\ y \geq h \\ G_{bb}^{2d}(x,y;x',y'), & y' < h,\ y < h \end{cases} \tag{2.44}$$

$$G_{aa}^{2d} = \frac{1}{4\pi\epsilon_1}\Bigg[\ln\frac{\Delta x^2 + (y+y')^2}{\Delta x^2 + \Delta y^2} + \sum_{k=1}^{\infty}\left(\frac{\epsilon_1-\epsilon_2}{\epsilon_1+\epsilon_2}\right)^k \ln\frac{\Delta x^2 + (y+y'+2kh)^2}{\Delta x^2 + (y+y'+2(k-2)h)^2}\Bigg] \tag{2.45}$$

$$G_{ab}^{2d} = \frac{1}{2\pi(\epsilon_1+\epsilon_2)}\sum_{k=0}^{\infty}\Bigg[\left(\frac{\epsilon_1-\epsilon_2}{\epsilon_1+\epsilon_2}\right)^k \ln\frac{\Delta x^2 + (y+y'+2kh)^2}{\Delta x^2 + (y-y'-2kh)^2}\Bigg] \tag{2.46}$$

$$G_{ba}^{2d} = \frac{1}{2\pi(\epsilon_1+\epsilon_2)} \sum_{k=0}^{\infty} \left[\left(\frac{\epsilon_1-\epsilon_2}{\epsilon_1+\epsilon_2} \right)^k \ln \frac{\Delta x^2 + (y+y'+2kh)^2}{\Delta x^2 + (y-y'+2kh)^2} \right] \tag{2.47}$$

$$\begin{aligned} G_{bb}^{2d} = \frac{1}{4\pi\epsilon_2} \Bigg[& \ln \frac{\Delta x^2 + (y+y')^2}{\Delta x^2 + \Delta y^2} \\ & + \sum_{k=1}^{\infty} \left(\frac{\epsilon_1-\epsilon_2}{\epsilon_1+\epsilon_2} \right)^k \ln \left\{ \frac{\Delta x^2 + (y+y'+2kh)^2}{\Delta x^2 + (y-y'+2kh)^2} \frac{\Delta x^2 + (y+y'-2kh)^2}{\Delta x^2 + (y-y'-2kh)^2} \right\} \Bigg] \end{aligned} \tag{2.48}$$

It is worth noting that by letting $\epsilon_1 \to \infty$ the homogeneous stripline configuration with ground plane separation h and permittivity ϵ_2 is recovered.

CHAPTER 3

THE METHOD OF MOMENTS AND NUMERICAL SOLUTION

In this chapter, the numerical solution of the integral equations formed in Chapter 2 is discussed. The method of moments is used to reduce the integral equations into a linear system of equations. Specifically, the point-matching method in conjuction with the subsectional method is utilized [Harrington, 1968]. This procedure is applied to both 2-D and 3-D problems. In addition, the discretization procedure along with relevant approximations are discused. Finally, the construction of the final matrix and the numerical computation of its entries are discussed.

3.1 The Method of Moments

The method of moments (MoM) is used for solving the integral equations (2.27) and (2.28). We define the following inner product

$$< \phi(\mathbf{r}), \psi(\mathbf{r}) > = \int_D \phi(\mathbf{r})\psi(\mathbf{r})\, d\Gamma \tag{3.1}$$

where D is the domain of interest, and ψ is a weight function.

It is assumed here that a suitable discretization has been performed. The details of this discretization will be discussed in the next section. A point matching procedure is chosen in order to reduce the integral equation into a linear system of equations. That is, Dirac delta functions located at the midpoint of each element

(line segment for 2-D case or sub-area for 3-D case) on the conductor surfaces are used as weight functions

$$\psi(\mathbf{r}) = \delta(\mathbf{r} - \mathbf{r}_n), \quad n = 1, \cdots, M_T. \tag{3.2}$$

where M_T is the total number of elements on all conductor surfaces. Pulse functions (subsectional method) are chosen as expansion functions. These functions have a value of unity on a particular subsection (element) and vanish on all other elements. We carry out the implementation of MoM for the 2-D and 3-D cases separately.

3.1.1 2-D Problem

Using the weighting functions of (3.2), the inner product of (3.1) is performed for both sides of (2.27). For instance, let $\mathbf{r}_n$ be the the position vector for the midpoint of the nth element on the surface of lth conductor. The weighting procedure with $\delta(\mathbf{r} - \mathbf{r}_n)$ yields

$$\sum_{i=1}^{N_C} \sum_{j=1}^{N_{S_i}} \left(\int_{W_{ij}} \hat{\sigma}_{ij}(\mathbf{r}') G^{2d}(\mathbf{r}_n, \mathbf{r}') d\ell' \right) = V_l \tag{3.3}$$

Let the unknown surface charge density on the jth side of the ith conductor be approximated as

$$\hat{\sigma}_{ij}(\mathbf{r}') = \sum_{k=1}^{M_{ij}} \hat{a}_k^{(ij)} P_k^{(ij)}(\mathbf{r}') \tag{3.4}$$

where M_{ij} is the number of elements on the jth side of the ith conductor, $\hat{a}_k^{(ij)}$ are unknown constants, and

$$P_k^{(ij)}(\mathbf{r}') = \begin{cases} 1, & \text{if } \mathbf{r}' \in \Delta L_k^{(ij)} \\ 0, & \text{otherwise.} \end{cases} \tag{3.5}$$

In the above $\Delta L_k^{(ij)}$ is the length of the kth segment on the jth side of the ith conductor. Substituting (3.4) and (3.5) into (3.3), we have

$$\sum_{i=1}^{N_C}\sum_{j=1}^{N_{S_i}}\sum_{k=1}^{M_{ij}} \hat{a}_k^{(ij)} \left(\int_{\Delta L_k^{(ij)}} G^{2d}(\mathbf{r}_n, \mathbf{r}')d\ell' \right) = V_l. \tag{3.6}$$

For simplicity, (3.6) is rewritten in the more compact form

$$\sum_{m=1}^{\hat{M}_T} \hat{Z}_{nm}\hat{b}_m = V_n \tag{3.7a}$$

where

$$\hat{Z}_{nm} = \int_{\Delta L_m} G^{2d}(\mathbf{r}_n, \mathbf{r}')d\ell', \tag{3.7b}$$

and the single summation is over all the elements on all conductors. $\hat{b}_m$ is the unknown constant surface charge density on the mth element, and $V_n = V_l$ is the contant potential of the nth element that is on the lth conductor. Repeating the above procedure for all $\hat{M}_T$ elements on the conducting surfaces of the geometry we obtain a linear system of $\hat{M}_T$ equations of the form (3.7a) for the $\hat{M}_T$ unknowns $\hat{b}_m$. In a matrix form we can write

$$\left[\hat{Z}\right]\left\{\hat{b}\right\} = \left\{V\right\} \tag{3.8}$$

The inversion of this linear system of equations completes the solution.

3.1.2 3-D Problem

The procedure in this case is similar to that for the 2-D case. The inner product is applied on both sides of (2.28) using the weighting functions of (3.2). The resulting equation for the nth element on the surface of the lth conductor is

$$\sum_{i=1}^{N_C}\sum_{j=1}^{N_{S_i}}\left(\int_{W_{ij}}\sigma_{ij}(\mathbf{r}')G^{3d}(\mathbf{r}_n,\mathbf{r}')d\ell'\right)=V_l-I^{-\infty}(\mathbf{r}_n)-I^{+\infty}(\mathbf{r}_n) \tag{3.9}$$

where again $\mathbf{r}_n$ is the position vector for the center of th nth element. Let the unknown surface charge density on the jth side of the ith conductor be approximated by

$$\sigma_{ij}(\mathbf{r}')=\sum_{k=1}^{M_{ij}}a_k^{(ij)}P_k^{(ij)}(\mathbf{r}') \tag{3.10}$$

where M_{ij} is the number of elements on the jth side of the ith conductor, $a_k^{(ij)}$ are unknown constants to be determined, and

$$P_k^{(ij)}(\mathbf{r}')=\begin{cases}1, & \text{if } \mathbf{r}'\in\Delta S_k^{(ij)}\\ 0, & \text{otherwise.}\end{cases} \tag{3.11}$$

In (3.11), $\Delta S_k^{(ij)}$ denotes the surface of the kth element on the jth side of the ith conductor. Substituting (3.10) and (3.11) into (3.9), we have

$$\sum_{i=1}^{N_C}\sum_{j=1}^{N_{S_i}}\sum_{k=1}^{M_{ij}}a_k^{(ij)}\left(\int_{\Delta W_k^{(ij)}}G^{3d}(\mathbf{r}_n,\mathbf{r}')d\ell'\right)=V_l-I^{-\infty}(\mathbf{r}_n)-I^{+\infty}(\mathbf{r}_n). \tag{3.12}$$

For simplicity, (3.12) is rewritten in the compact form

$$\sum_{m=1}^{M_T}Z_{nm}b_m=\tilde{V}_n \tag{3.13a}$$

where

$$Z_{nm} = \int_{\Delta W_m} G^{3d}(\mathbf{r}_n, \mathbf{r}')d\ell', \tag{3.13b}$$

$$\tilde{V}_n = V_l - I^{-\infty}(\mathbf{r}_n) - I^{+\infty}(\mathbf{r}_n) \tag{3.14a}$$

and

$$I^{-\infty}(\mathbf{r}_n) = \sum_{m=1}^{\hat{M}_T} \hat{b}_m \int_{\Delta L_m} G^{-\infty}(\mathbf{r}_n, \mathbf{r}')d\ell', \tag{3.14b}$$

$$I^{+\infty}(\mathbf{r}_n) = \sum_{m=1}^{\hat{M}_T} \hat{b}_m \int_{\Delta L_m} G^{+\infty}(\mathbf{r}_n, \mathbf{r}')d\ell', \tag{3.14c}$$

The summation in (3.13a) is over all elements M_T of the conductors. V_l is the constant potential of the lth conductor which contains the nth element, and b_m is the unknown constant surface charge density on the mth element. The summations in (3.14b,c) are the contribution from the semi-infinite lines which have known charge distributions. As already mentioned, these charge distributions are calculated using the 2-D procedure of Section 3.1.1. Repeating the testing procedure for all the elements, we obtain a linear system of M_T equations of the form (3.13a), which in matrix form is

$$\left[Z\right]\left\{b\right\} = \left\{\tilde{V}\right\} \tag{3.15}$$

The inversion of this system of equations completes the solution.

3.2 Discretization Procedure

Both (3.7a) and (3.13a) demand appropriate discretization of the conductor surfaces. In this section, the discretization procedure for the 2-D and 3-D cases will be discussed. All of the conductor contours are divided into straight line segments (2-D case) or rectangular sub-areas (3-D case).

3.2.1 2-D Discretization

In the 2-D case, all structures must be of rectangular shape and the sides must be either parallel or perpendicular to the dielectric interface (see Figure 2–2). Assuming that the four vertices of each conductor (ith conductor in this case) and the number of subsections (M_{ij}) on each side (j) are known, each conductor is discretized in the following manner.

Starting from lower left corner and counting counter clockwise, we assign numbers 1 through 4 to the vertices and sides, each side having the same number as the preceeding vertex as shown in Figure 3–1. Then, for the ith conductor each segment on side 1 (j=1) is characterized by the following variables

$$\Delta L_m^{(i1)} = \frac{x_2 - x_1}{M_{i1}} \tag{3.16a}$$

$$x_{c_m} = x_1 + m\frac{\Delta L_m^{(i1)}}{2} \tag{3.16b}$$

$$y_{c_m} = y_1 \tag{3.16c}$$

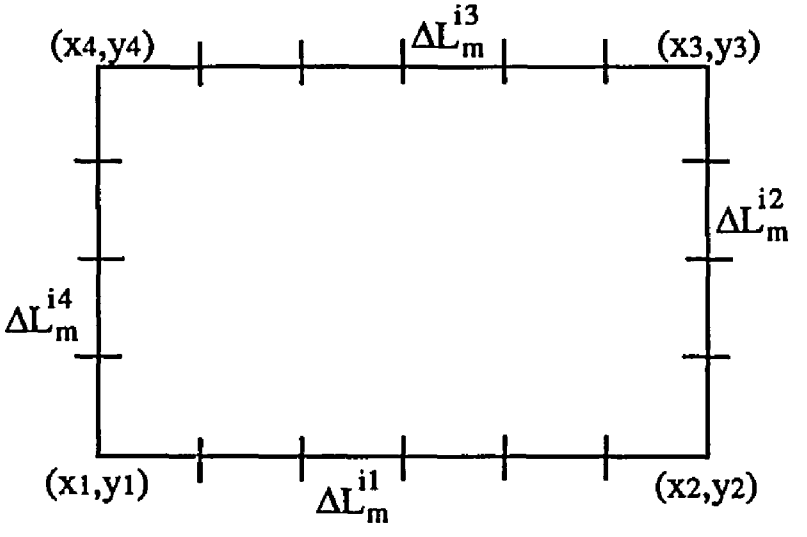

Figure 3-1 Two-dimensional discretization scheme.

for $m = 1, \cdots, M_{i1}$. For segments on side 2 (j=2)

$$\Delta L_m^{(i2)} = \frac{y_3 - y_2}{M_{i2}} \tag{3.17a}$$

$$x_{c_m} = x_2 \tag{3.17b}$$

$$y_{c_m} = y_2 + m\frac{\Delta L_m^{(i2)}}{2} \tag{3.17c}$$

for $m = 1, \cdots, M_{i2}$. Similarly, the subsections on side 3 (j=3) are characterized by

$$\Delta L_m^{(i3)} = \frac{x_4 - x_3}{M_{i3}} \tag{3.18a}$$

$$x_{c_m} = x_3 + m\frac{\Delta L_m^{(i3)}}{2} \tag{3.18b}$$

$$y_{c_m} = y_3 \tag{3.18c}$$

where $m = 1, \cdots, M_{i3}$. Finally, for the fourth side (j=4) we have

$$\Delta L_m^{(i4)} = \frac{y_1 - y_4}{M_{i4}} \tag{3.19a}$$

$$x_{c_m} = x_4 \tag{3.19b}$$

$$y_{c_m} = y_4 + m\frac{\Delta L_m^{(i4)}}{2} \tag{3.19c}$$

for $m = 1, \cdots, M_{i4}$. In all the above equations (x_{c_m}, y_{c_m}) is the midpoint of the mth subsection. The above data and the orientation (parallel to x axis or y axis) of each segment suffice for the numerical computation.

3.2.2 3-D Discretization

The discretization of the conductor surfaces was performed in the following manner. With each conductor side assumed to be an arbitrary quadrilateral with all four vertices on the same plane, a local cartesian coordinate system (p, q) is defined with its q axis parallel to the longest side of the quadrilateral that is not parallel with the y axis (see Figure 3–2). The relationship between the global and local coordinates is given by

$$q = (z - z_0)cos\theta + (x - x_0)sin\theta \tag{3.20a}$$

$$p = (x - x_0)cos\theta - (z - z_0)sin\theta \tag{3.20b}$$

where

$$x_0 = \frac{1}{4}(x_1 + x_2 + x_3 + x_4) \tag{3.21a}$$

$$z_0 = \frac{1}{4}(z_1 + z_2 + z_3 + z_4) \tag{3.21b}$$

and θ is angle between the longest side and the z axis. In addition, a generic local coordinate system (u, v) is defined the following way.

If the conductor side is parallel to the dielectric interface (xz plane), then

$$u \equiv p \tag{3.22a}$$

$$v \equiv q \tag{3.22b}$$

otherwise when the conductor side is perpendicular to the interface, we define

$$u \equiv y \tag{3.23a}$$

$$v \equiv q \tag{3.23b}$$

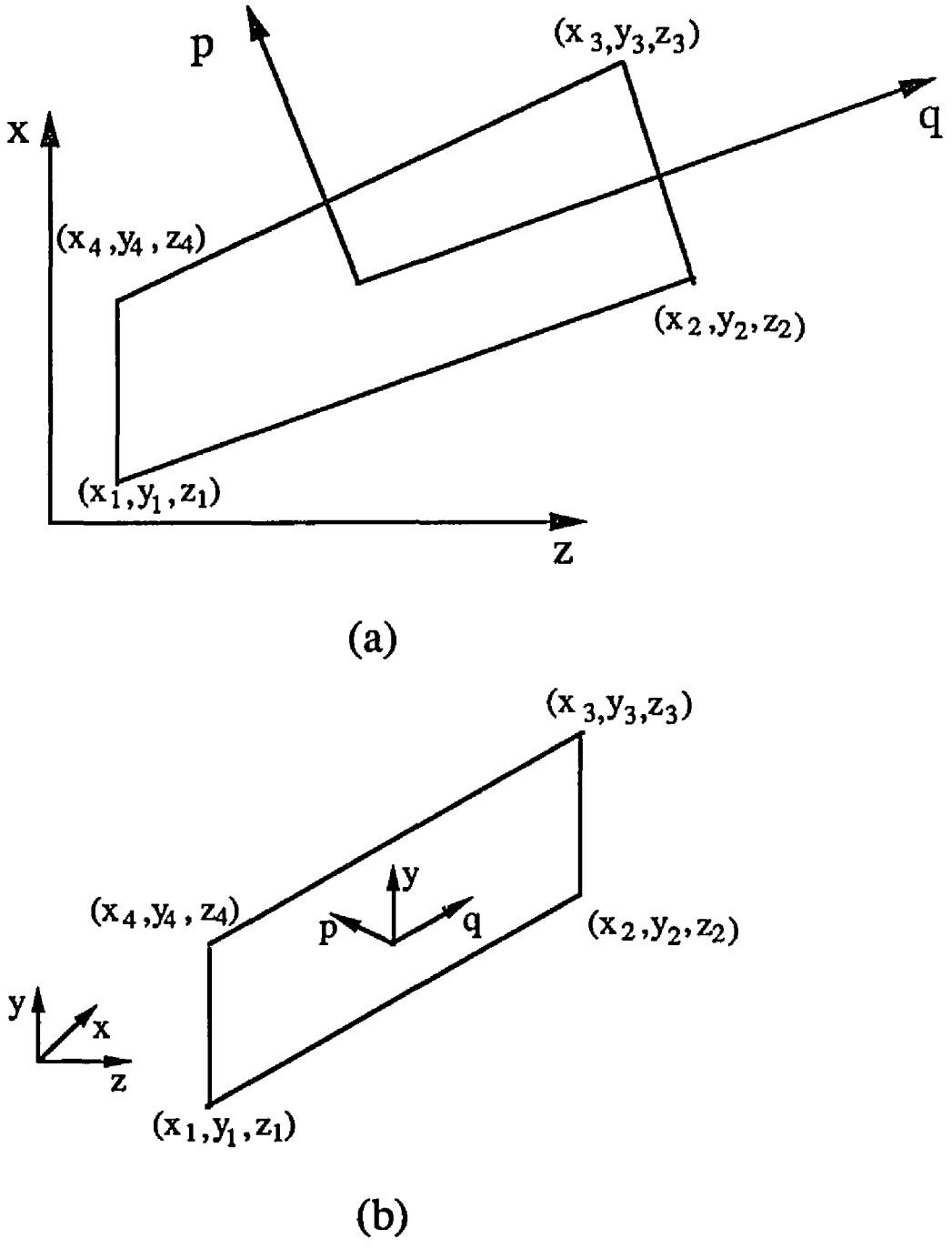

Figure 3-2 An illustration of the (p, q) coordinate system: (a) surface parallel to the xz plane; (b) surface perpendicular to the xz plane.

It is well-known that a local, non-orthogonal coordinate system (ξ, η), centered at the barycenter of the quadrilateral, can be defined in such a way that one particular coordinate has value ± 1 at one node of the quadrilateral and zero value at the other nodes, while its variation between nodes is linear [Huebner, 1975]. The mapping from (ξ, η) to (u, v) is given in terms of the coordinates of the four vertices of the quadrilateral (u_i, v_i), $i = 1, \ldots, 4$, as

$$u = \frac{1}{4} \sum_{i=1}^{4} (1 + \xi\xi_i)(1 + \eta\eta_i) u_i \tag{3.24a}$$

$$v = \frac{1}{4} \sum_{i=1}^{4} (1 + \xi\xi_i)(1 + \eta\eta_i) v_i \tag{3.24b}$$

The above equations suggest the following discretization procedure. First, a rectangular grid is generated over the map of the quadrilateral under study as shown in Figure 3–3b. Then, (3.24a) and (3.24b) are used to map the nodes of the rectangular grid to the (u, v) plane as shown in Figure 3–3a. Finally, each element generated from the above procedure is approximated by the rectangle obtained from the intersection of the four lines drawn through the center points of the four sides of the element parallel to the coordinate axes as illustrated in Figure 3–4. This way, the line charge Green's functions introduced earlier can be utilized to reduce the two-dimensional element integrations to one-dimensional. This geometry approximation is expected to be adequate for quadrilaterals with inner angles within the range $[\pi/4, 3\pi/4]$. The accuracy of this approximatin is discussed in Section 3.4.

3.3 Numerical Evaluation of the Integrals

In this section we will discuss the numerical calculation of the integrals involved in the MoM solution.

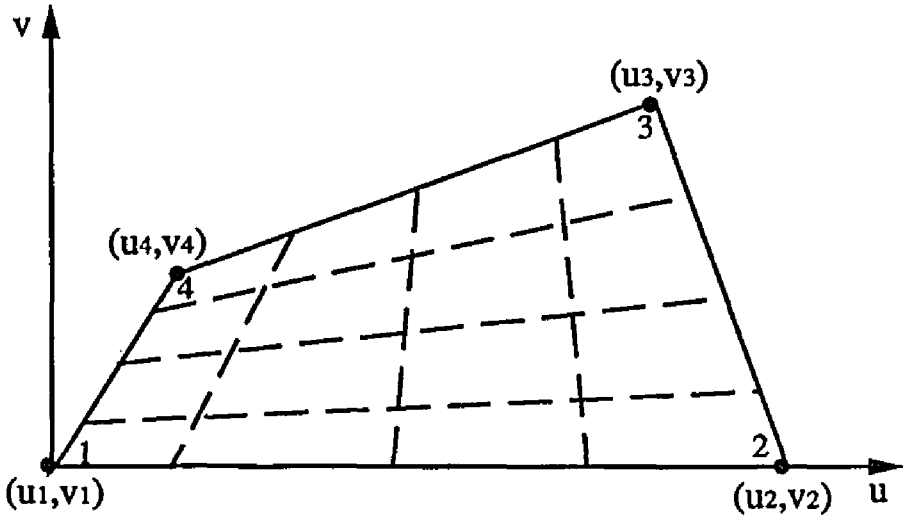

(a)

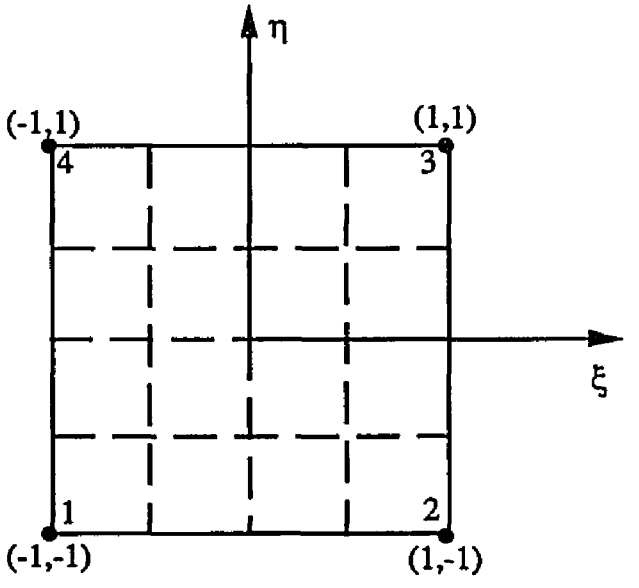

(b)

Figure 3-3 (a) Conductor sides can be of arbitrary quadrilateral shapes; (b) the map of the quadrilateral on the $\xi\eta$-plane.

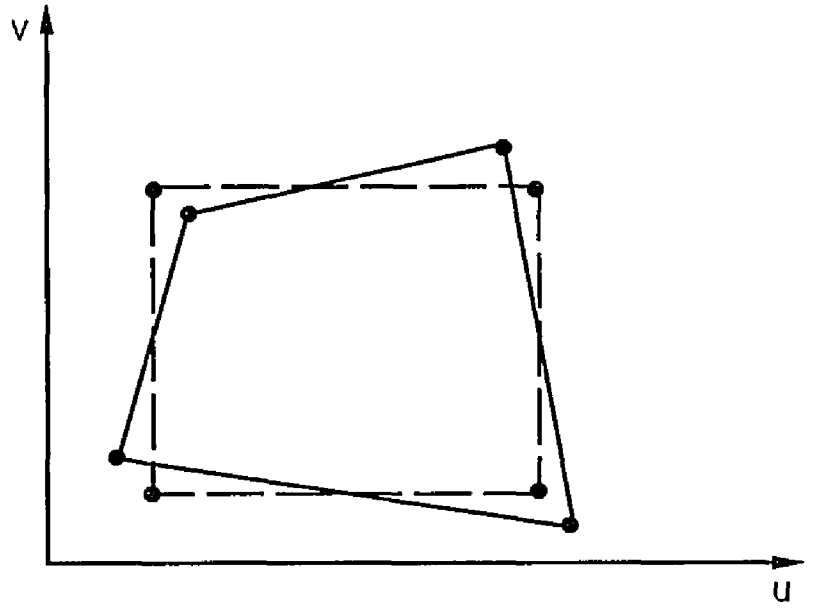

Figure 3-4 Element approximation for numerical calculations. Original element in solid lines and approximating element in dashed lines.

3.3.1 Evaluation of $\hat{Z}_{nm}$

If the discretization is fine enough, then the integration in the expressions for $\hat{Z}_{nm}$ can be approximated by the product of the integrand calculated at the midpoint of the mth element and the length ΔL_m, provided that $n \neq m$.

$$\hat{Z}_{nm} = G^{2d}(x_{c_n}, y_{c_n}, x_{c_m}, y_{c_m}) \cdot \Delta L_m, \;\; n \neq m \tag{3.25}$$

For the selfterm case ($n = m$), a numerical integration is performed. For example, if the mth element is on a surface parallel to the x axis

$$\begin{aligned} \hat{Z}_{mm} &= \int_{\Delta L_m} G^{2d}(x_{c_m}, y_{c_m}, x', y_{c_m}) dx' \\ &= \frac{\Delta x_m}{2} \int_{-1}^{1} G^{2d}(x_{c_m}, y_{c_m}, x'(\zeta), y_{c_m}) d\zeta \end{aligned} \tag{3.26a}$$

where

$$x'(\zeta) = \frac{\Delta x_m}{2}(\zeta + 1) + x_m^a \tag{3.26b}$$

where x_m^a is the smaller end point of the mth segment. There is a singularity in (3.26a) at $x' = x_{c_m}$ or $\zeta = 0$. In order to effectively account for the singularity, the non-linear transformation given in [Telles, 1987] is employed. This transformation concentrates more integration points at the vicinity of the singularity. In this particular case, the transformation is $\zeta = \gamma^3$. Thus,

$$\hat{Z}_{mm} = \frac{3}{2}\Delta x_m \int_{-1}^{1} G^{2d}(x_{c_m}, y_{c_m}, x'(\gamma^3), y_{c_m}) \gamma^2 d\gamma. \tag{3.27}$$

The numerical evaluation of the integral in (3.27) is accomplished by applying ten-point Guassian quadrature as shown below

$$\hat{Z}_{mm} = \frac{\Delta x_m}{2} \sum_{l=1}^{5} \Big\{ \Big[G^{2d}(x_{c_m}, y_{c_m}, x'(\gamma_l{}^3), y_{c_m}) + G^{2d}(x_{c_m}, y_{c_m}, x'(-\gamma_l{}^3), x_{c_m}) \Big] \gamma_l{}^2 w_l \Big\} \tag{3.28}$$

where the γ_l are the tranformed coordinates of the quadrature points in the interval $-1 \leq \gamma \leq 1$; and the w_l are the associated weights. Even number of quadrature points must be chosen so that none of the quadrature points coincides with the singularity. The coordinates of the quadrature points and associated weights are tabulated in [Abramowitz and Stegun, 1972]. When the mth element is on a surface that is parallel to the y axis, y' is used as the variable of integration and the above procedure is followed.

3.3.2 Evaluation of Z_{nm}

With the assumption that the discretization is fine enough, the integral of Z_{nm}, $n \neq m$, can be approximated by the product of the integrand calculated at the midpoint of the mth element and the width ΔW_m. The Green's function G^{3d} corresponds to the potential due to a line charge of length $\Delta \ell_m$, which is the length of the rectangle approximating the mth element as shown on Figure 3–5. In the following computations, the local coordinate system (p, q) of the side on which the mth element resides is used. Let the mth rectangular element extend from $q^a_{c_m}$ to $q^b_{c_m}$, then

$$\Delta \ell_m = \Delta q_m = q^b_{c_m} - q^a_{c_m}. \tag{3.29a}$$

However, in order to conserve the area ΔS_m of the original element and hence the total surface area of the conductor, we calculate the width as

$$\Delta W_m = \frac{\Delta S_m}{\Delta \ell_m}. \tag{3.29b}$$

Thus, Z_{nm} is approximated by

$$Z_{nm} = G^{3d}(p_{c_n}, y_{c_n}, q_{c_n}, p_{c_m}, y_{c_m}, q^a_{e_m}, q^b_{e_m}) \cdot \Delta W_m, \;\; n \neq m \tag{3.30}$$

where $(p_{c_n}, y_{c_n}, q_{c_n})$ is the center point of the nth element and $q^a_{e_m}$ and $q^b_{e_m}$ are the end points of the line source centered at (p_{c_m}, y_{c_m}).

When $n = m$, a singularity occurs at the center of the element. In this case, a numerical integration is performed in a manner similar to that for $\hat{Z}_{mm}$. Let the mth element be on a surface parallel to the dielectric interface and let the approximating rectangle extending from p^a_m to p^b_m. Then

$$\begin{aligned} Z_{mm} &= \int_{\Delta W_m} G^{3d}(p_{c_m}, y_{c_m}, q_{c_m}, p', y_{c_m}, q^a_{e_m}, q^b_{e_m}) dp' \\ &= \frac{\Delta W_m}{2} \int_{-1}^{1} G^{3d}(p_{c_m}, y_{c_m}, q_{c_m}, p'(\zeta), y_{c_m}, q^a_{e_m}, q^b_{e_m}) d\zeta \end{aligned} \tag{3.31a}$$

where

$$p'(\zeta) = \frac{\Delta p_m}{2}(\zeta + 1) + p^a_m \tag{3.31b}$$

$$\Delta p_m = p^b_m - p^a_m \tag{3.31c}$$

A singularity occurs at $p' = p_{c_m}$ or $\zeta = 0$. For efficient numerical computation, we use the non-linear transformation $\zeta = \gamma^3$, thus

$$Z_{mm} = \frac{3}{2}\Delta p_m \int_{-1}^{1} G^{3d}(p_{c_m}, y_{c_m}, q_{c_m}, p'(\gamma^3), y_{c_m}, q^a_{e_m}, q^b_{e_m}) \gamma^2 d\gamma \tag{3.32}$$

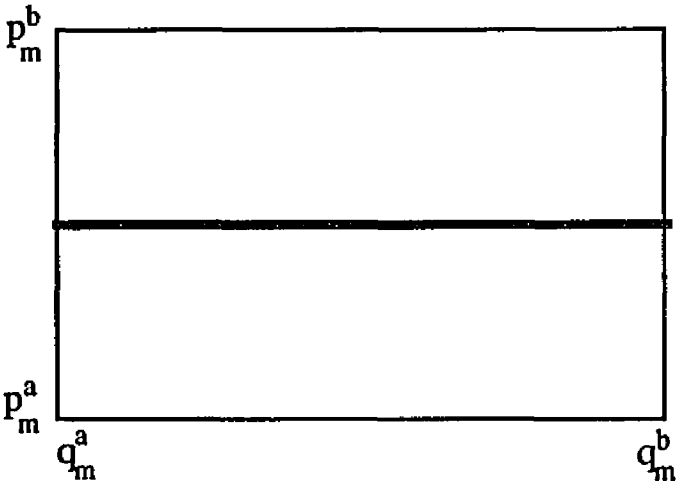

Figure 3-5 The rectangular element used for numerical calculations. The thick solid line represents the line charge.

Applying ten-point Gaussian quadrature, we obtain

$$Z_{mm} = \frac{3}{2}\Delta p_m \sum_{l=1}^{5}\Big\{\Big[G^{3d}(p_{c_m}, y_{c_m}, q_{c_m}, p'(\gamma_l{}^3), y_{c_m}, q^a_{e_m}, q^b_{e_m}) + G^{3d}(p_{c_m}, y_{c_m}, q_{c_m}, p'(-\gamma_l{}^3), y_{c_m}, q^a_{e_m}, q^b_{e_m})\Big]\gamma_l{}^2 w_l\Big\} \tag{3.33}$$

where γ_l, w_l are abscissas and weights of the Gaussian integration, respectively. If the mth element is on a surface that is parallel to the y axis, then y' is the variable of integration and we obtain

$$Z_{mm} = \frac{3}{2}\Delta y_m \sum_{l=1}^{5}\Big\{\Big[G^{3d}(p_{c_m}, y_{c_m}, q_{c_m}, p_{c_m}, y'(\gamma_l{}^3), q^a_{e_m}, q^b_{e_m}) + G^{3d}(p_{c_m}, y_{c_m}, q_{c_m}, p_{c_m}, y'(\gamma_l{}^3), q^a_{e_m}, q^b_{e_m})\Big]\gamma_l{}^2 w_l\Big\} \tag{3.34}$$

3.3.3 Evaluation of $I^{-\infty}$ and $I^{+\infty}$

Evaluation of the two integrals appearing in (3.14b,c) is essentially the same; the only difference is that a different Green's function is used. Since $\mathbf{r}_n$ is the center point of an element at some distance away from the contour of integration along the discrete line segments, there is no singularity present. Using a linear coordinate transformation onto the natural coordinate γ, $-1 \leq \gamma \leq 1$, we use ten-point Gaussian quadrature for the numerical integration. For example, $I^{-\infty}(\mathbf{r}_n)$ is calculated as

$$I^{-\infty}(\mathbf{r}_n) = \sum_{m=1}^{M_T}\Big\{\hat{b}_m \frac{\Delta L_m}{2}\sum_{l=1}^{5}\Big[G^{-\infty}(\mathbf{r}_n, x^+, y^+, z_2) + G^{-\infty}(\mathbf{r}_n, x^-, y^-, z_2)\Big]w_l\Big\} \tag{3.35}$$

where $x^+ = x'(\gamma_l)$, $x^- = x'(-\gamma_l)$, and $y^- = y^+ = y_{c_m}$ for the case the mth line segment is parallel with the x axis; for the other case, ΔL_m is parallel with the y axis $y^+ = y'(\gamma_l)$, $y^- = y'(-\gamma_l)$, and $x^- = x^+ = x_{c_m}$. And of course, $I^{+\infty}(\mathbf{r}_n)$ is approximated similarly.

3.4 Computational Aspects

3.4.1 Element approximations

The accuracy and validity of the element approximation procedure discussed in Section 3–2 will be evaluated in this section. Consider a plane disk of area A and radius r ($A = \pi r^2$), which has a uniform charge density of a unit amplitude and is located at a height h above a ground plane. This situation is shown on Figure 3–6. The electrostatic potential at its center is given by

$$\phi_{center} = \int_0^{2\pi} d\theta \int_0^r \rho d\rho \frac{1}{4\pi\epsilon} \left(\frac{1}{\rho} - \frac{1}{\sqrt{\rho^2 + (2h)^2}} \right) \tag{3.36}$$

Analytical evaluation of the above integral gives

$$\phi_{center} = \frac{1}{2\epsilon} \left[\sqrt{\frac{A}{\pi}} - \left(\sqrt{\frac{A}{\pi} + 4h^2} - 2h \right) \right] \tag{3.37}$$

We compare this potential to the potential obtained at the center of various rectangles of different aspect ratios a/b (see Figure 3–7), associated with uniform charge densities of unit amplitude over the rectangle. All rectangles are at height h above

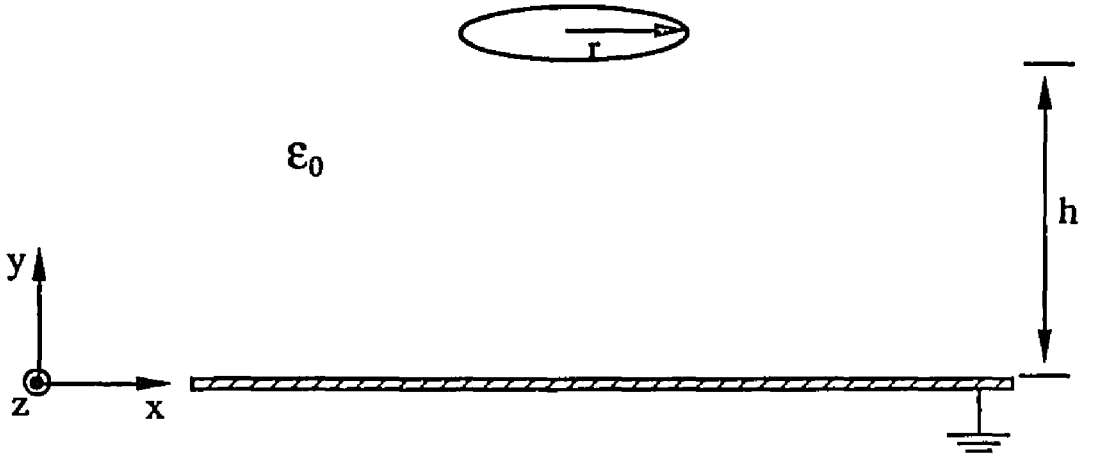

(a)

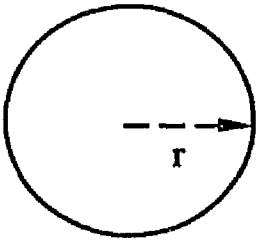

(b)

Figure 3-6 A uniformly charged disk, with area A and radius r, located above a ground plane .

the ground plane and have the same area A equal to that of the circular disk. Considering the rectangle as one element and utilizing formulations developed in the previous sections, we have

$$\phi'_{center} = Z_{mm} \tag{3.38}$$

where Z_{mm} is given in (3.33) and $m = 1$.

Let the plates be in free space (ϵ=ϵ_0) and A=h=1, then $\phi_{center} = 2.74528 \times 10^{10}$ for the circular disk. On the other hand, $\phi'_{center} = 2.73832 \times 10^{10}$ for a square ($a = b = 1$); $\phi'_{center} = 2.34593 \times 10^{10}$ for a rectangle with $a = \frac{1}{2}$, $b = 2$; and $\phi'_{center} = 1.61365 \times 10^{10}$ for a rectangle with $a = \frac{1}{4}$, $b = 4$. From these results it is evident that the ϕ_{center} is approximated best by using the square element (0.25% difference).

From Figure 3–7, we note that the narrower the rectangle the smaller the overlap between the rectangle and the disk. In fact, we may say that as the intersection between the two elements decreases, the approximation of one by the other gets worse even if they have the same center and area. This argument can be extended to the approximation of a general quadrilateral by a rectangle. As shown in Figure 3–8, it is clear that the quadrilateral with inner angles outside the range $[\pi/4, 3\pi/4]$ can not be adequately approximated by a rectangle.

Nevertheless, we expect not to encounter such quadrilaterals in the geometries under consideration in this work.

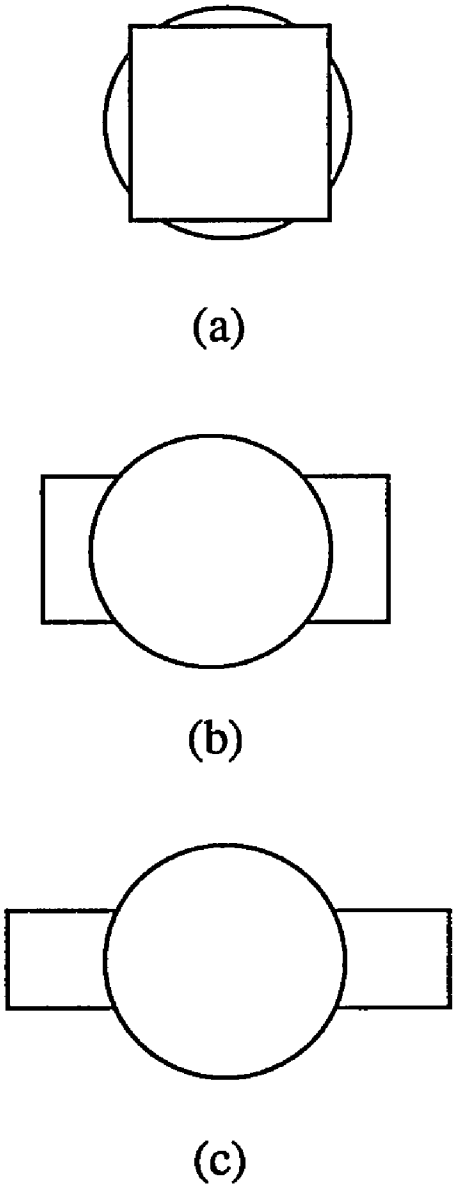

Figure 3-7 Approximations of the disk with: (a) a square; (b) a rectagle with $\frac{a}{b}=\frac{1}{4}$; (c) a rectagle with $\frac{a}{b}=\frac{1}{16}$.

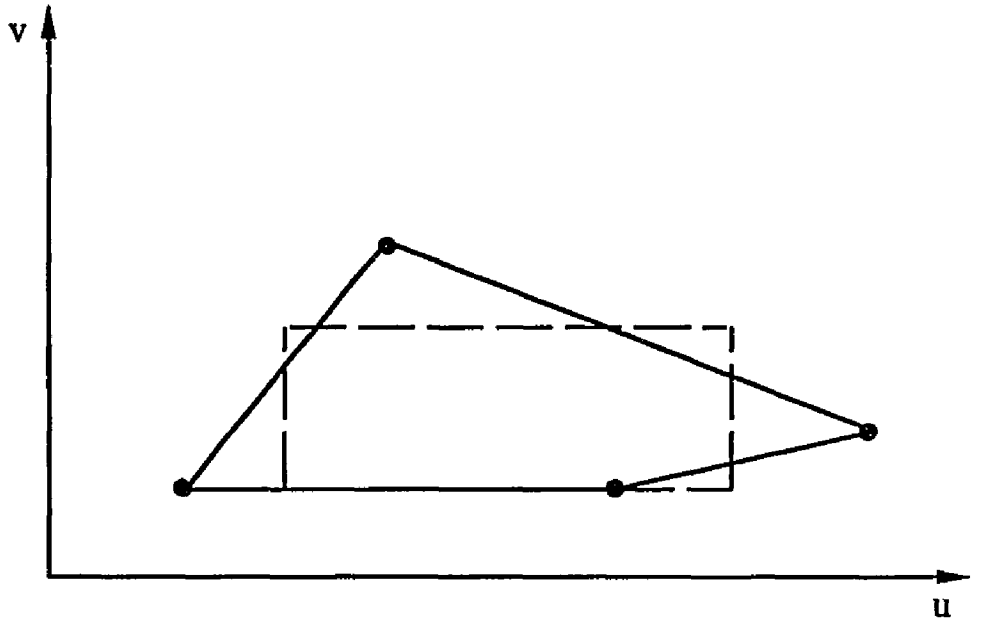

Figure 3-8 An ill-posed approximation of an arbitrary quadrilateral by a rectangle.

3.4.2 Number of elements

Consider a square conducting plate in free space above a ground plane, with dimensions h=w=1cm, as shown in Figure 3–9. We wish to determine how many elements are necessary to efficiently compute the capacitance of this geometry by using the previously developed formulation. Let N_U and N_V be the number of elements along the u and v axes, respectively. Since we choose the line charges to be parallel with the v axis, the numerical integration is carried out with respect to u.

We plot the capacitance as a function of N_U ($1 \leq N_U \leq 15$) for several values of N_V (N_V=1,3,5,8,10). The plot is shown in Figure 3–10. From these curves we can deduce that $3 \leq N_V \leq 8$ and $7 \leq N_U \leq 12$ are good discretization values for efficient computation of the capacitance. We also notice that rectangles with their longer side parallel to the v axis (i.e. $N_V \leq N_U$) give more accurate results.

In order to validate the formulation, we used another 3-D capacitance calculator, MOM3D [Scheinfein and Palusinski, 1987]. For $N_U = N_V = 5$, the capacitance obtained from MOM3D is 0.458pf. And for $N_U = N_V = 10$, we obtained a capacitance value of 0.475pf. We see that these results are consistant with our results in Figure 3–10.

3.4.3 Approximation of a non-rectangular surface

A good test for the accuracy of our method of approximation for non-rectangular surfaces is discussed here. We calculate the capacitance of a square microstrip patch above a substrate of thickness 0.5mm and $\epsilon_r = 4$ as shown in Figure 3–11a. We obtained a capacitance of 0.28193pf for the square when $N_V = 5$

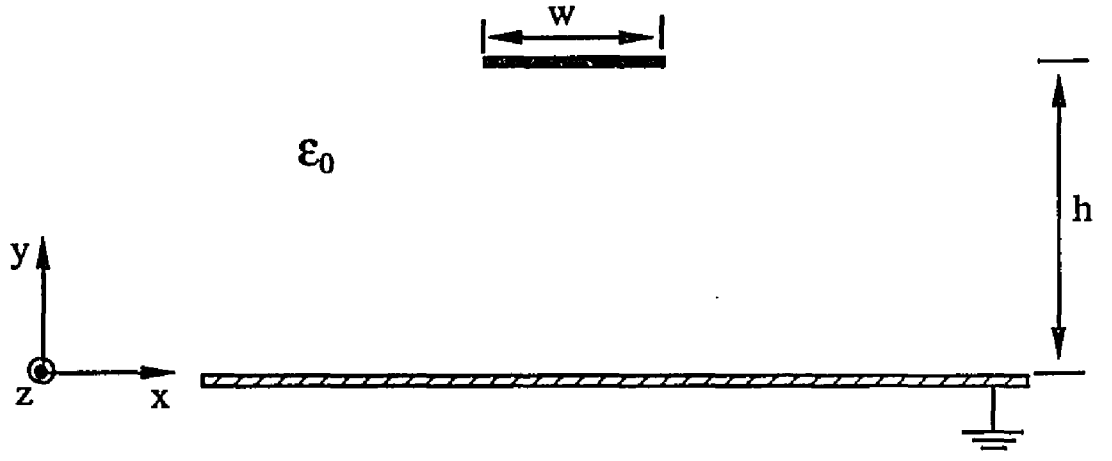

(a)

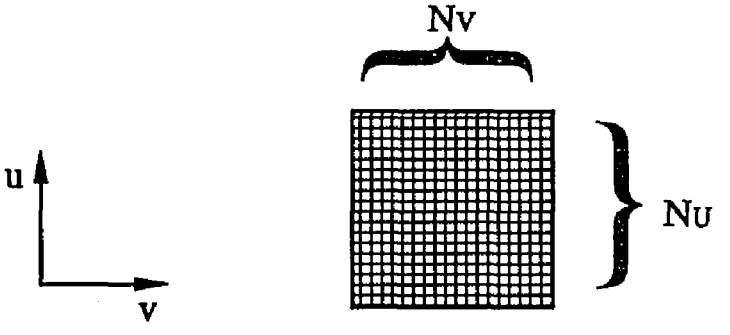

(b)

Figure 3-9 The square that is used for the discretization study.

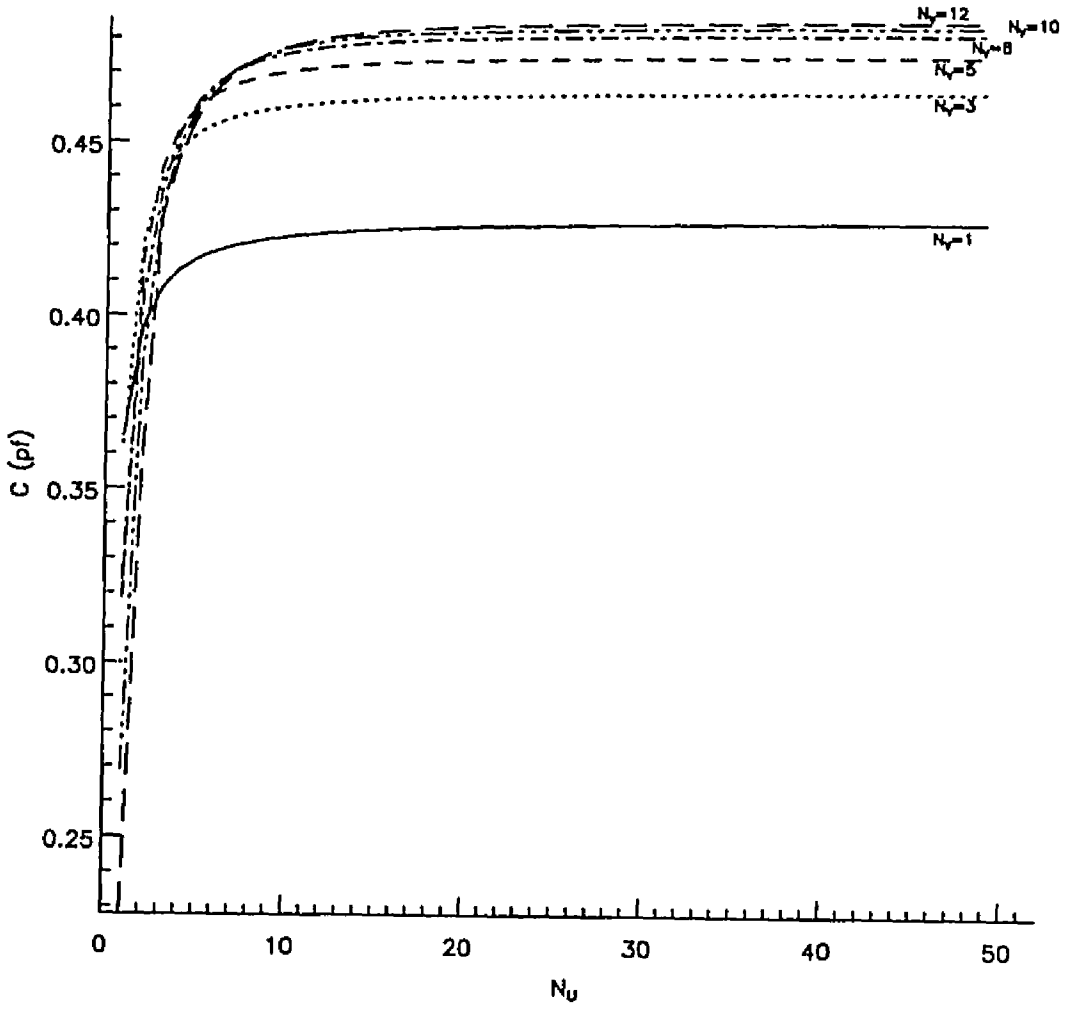

Figure 3-10 Graph of capacitance vs. number of elements per side.

and $N_U = 10$. We then split the square into two non-rectangular quadrilaterals as shown in Figure 3–11b and computed the capacitance of the combination of the two quadrilaterals with $N_V = N_U = 5$ for each quadrilateral. A capacitance of 0.27832pf was obtained in this case. Comparing this capacitance with the previous one, we obtained a difference of ~1.28%. From these results it is evident that this method of approximation is reliable.

3.4.4 Capacitance of an infinitely long line

The usage of semi-infinite lines for the regions of conductors extending to infinity is now examined. An infinitely long microstrip of rectangular cross section, width of 2.5cm and thickness of 1cm, is the subject of our evaluation (see Figure 3–12a). The capacitance of this strip can be calculated using a two-dimensional analysis. For the geometry shown in Figure 3–12a, p.u.l. capacitance of 8.1936pf/cm is obtained. Next, the long strip is split into three sections: a finite length section, a section extending to $-\infty$, and a section extending to $+\infty$ as shown in Figure 3–12b. Let L be the length of the finite section. We then calculate the p.u.l. capacitance C_{pul} of the finite section for three different lengths (L). For L=20cm, C_{pul}=8.1899pf/cm is obtained. Moreover, for L values of 10cm and 2cm, C_{pul}=8.1743pf/cm and C_{pul}=8.1596pf/cm are obtained, respectively. As a matter fact, when L=2cm the length of the section is smaller than the width of the conductor and still only a ~0.42% error is made compared with the two-dimensional result.

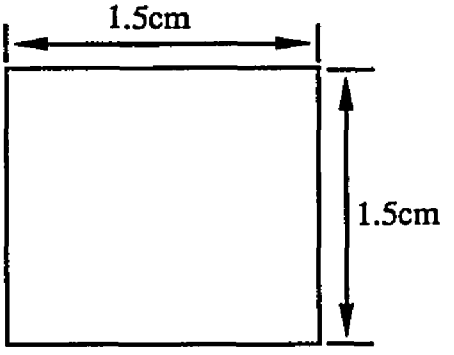

(a)

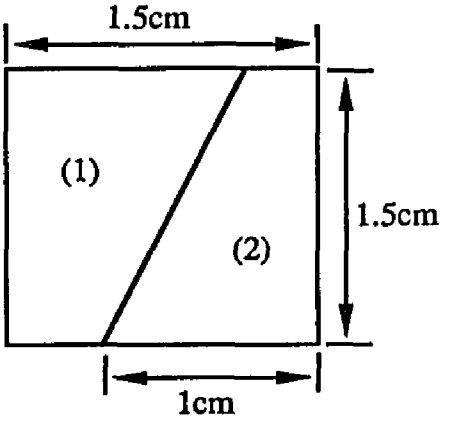

(b)

Figure 3-11 (a) Complete square; (b) devided square consisting of two non-rectangular quadrilterals.

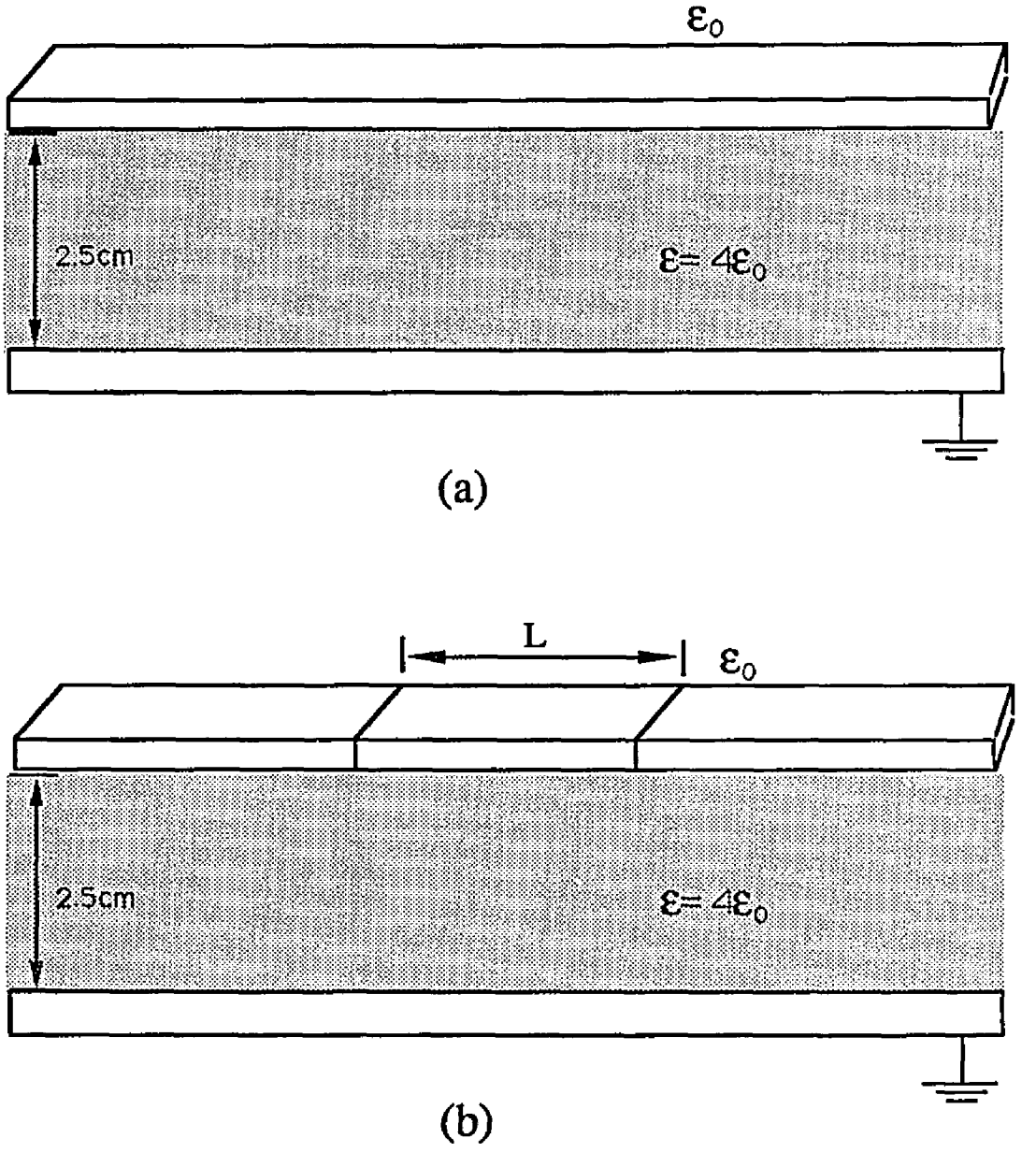

Figure 3-12 (a) Infinitely long line; (b) combination of two semi-infinite lines and a finite line.

CHAPTER 4

APPLICATIONS

A FORTRAN computer program (called UA3DC) was developed based on the algorithm discussed in the previous chapters. This program is designed to calculate the capacitance and/or the p.u.l. capacitance of arbitrary three-dimensional multi-conductor configurations of the microstrip and the stripline type. This program will be applied to several problems in this chapter. Some of these are simple examples and are used to test the validity of the formulation and the program. Other more complicated applications include computation of p.u.l. capacitance of coupled, flaring microstrip lines, and the extraction of the excess capacitances for a via, coupled conductor bends, and conductor crossovers.

4.1 The Capacitance of a Rectangular Conducting Box

In order to test the mathematical formulation and the validity of the program, the simple rectangular geometry of Figure 4–1 was analyzed. The perfectly conducting rectangular box was placed at a distance h=1cm from a ground plane of infinite extent. The cross-sectional dimensions were chosen as a=b=1cm, while the length l was varied between the values of 1cm and 50cm. The values for the capacitance of the box obtained using this approach, C, were compared with the capacitances calculated using the free space Green's function approach, C^*, [Scheinfein and Palusinski, 1987], and excellent agreement was observed as shown below.

l (cm)	C (pf)	C^* (pf)
1.0	0.93	0.86
5.0	2.38	2.28
20.0	7.62	7.36
50.0	18.04	17.45

It is interesting to notice that the maximum difference between the two methods, (~7%), is obtained for $l = 1$ cm. This is due to the fact that the singularity of the charge density at the conductor edges (edge effect) has a more profound effect on the capacitance of the box for lengths l comparable to the cross-sectional dimensions. The two methods use different schemes for the discrete approximations of the charge distributions on the conductors; hence, the discrepancy in their results is expected to be larger for such values of l. However, as the length l increases, the effect of the singularity of the charge density at the edges on the total charge is not as significant, and the results of the two methods are in better agreement (~3%).

4.2 Lumped Circuit Representation of Discontinuities

Interconnections are usually modeled as transmission lines so that the simplistic transmission line theory can be applied. Each transmission line is characterized by a p.u.l capacitance and a p.u.l. inductance which is found from the p.u.l. capacitance as discussed in Section 2.1. The interconnection conductor shown in Figure 4–2a is represented by the equivalent circuit shown in Figure 4–2b. The discontinuity located between the planes PP' and QQ' is represented by the lumped elements C_{ex} and L_{ex}. The two uniform sections, one between AA' and PP' and the other between QQ' and BB', are represented by uniform transmission lines with the

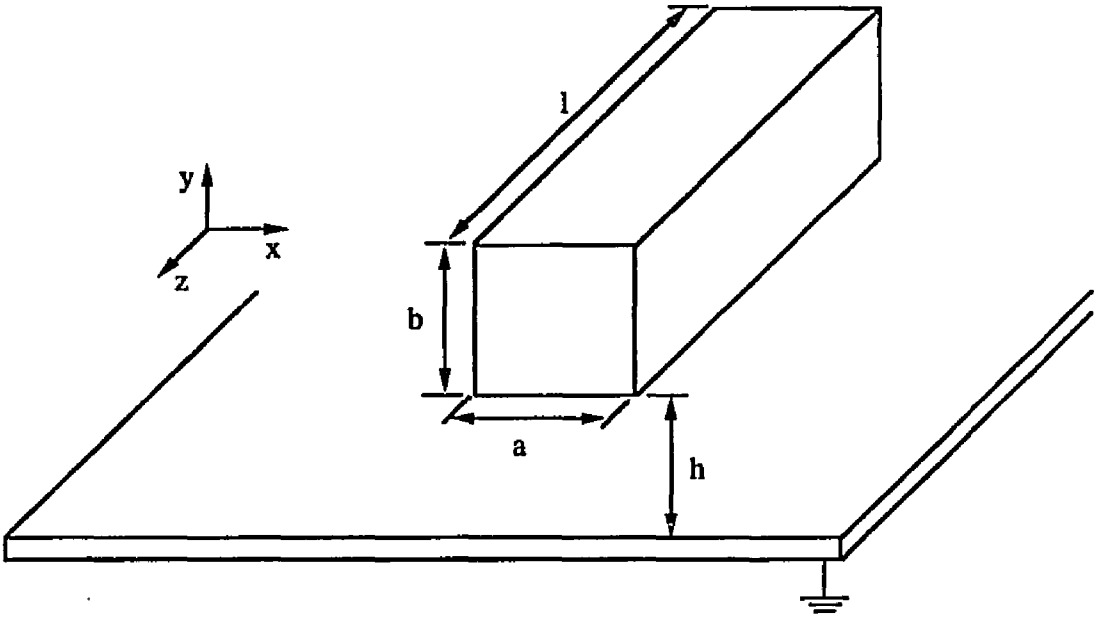

Figure 4-1 Single conductor above infinite ground plane.

same p.u.l. capacitance and inductance as the sections they represent. The excess capacitance C_{ex} and inductance L_{ex} are

$$C_{ex} = C_T - C_1 l_1 - C_2 l_2 \tag{4.1}$$

$$L_{ex} = L_T - L_1 l_1 - L_2 l_2 \tag{4.2}$$

where C_T and L_T are the total capacitance and inductance of the conductor between the planes AA' and BB'. C_T is obtained from the 3D analysis developed in this work, where L_T is found from a magnetostatic problem as discussed in [Cangellaris et al, 1990]. (C_1, L_1) and (C_1, L_1) are the p.u.l. capacitance and inductance obtained from 2-D analysis for lines (1) and (2), respectively. Here, we are only concerned with obtaining C_{ex}. In the following examples we will calculate C_{ex} for several discontinuities.

4.2.1 A Via

A via of finite length is depicted in Figure 4–3a. For the case A=B=T=1cm and H_1=H_2=1cm, the p.u.l. capacitance (C_{pul}) of this structure is given in [Scheinfein and Palusinski, 1987] and reproduced in Figure 4–3b. A similar calculation is carried out here and a plot of C_{pul} in the z direction is shown in Figure 4–4. As seen from these plots there is very good agreement between the two results. As expected the capacitance reaches a relative maximum value at the via (12cm$\leq$ z $\leq$13cm). The area under the curve is the so called excess capacitance (C_{ex}) which can be found by (4.1). Let us define the discontinuity to be between 12cm and 13cm. For this case, l_1=l_2=12cm, C_T=8.11788pf, C_1=0.34885pf/cm, and C_2=0.24841pf/cm. Hence, C_{ex}=0.95076pf.

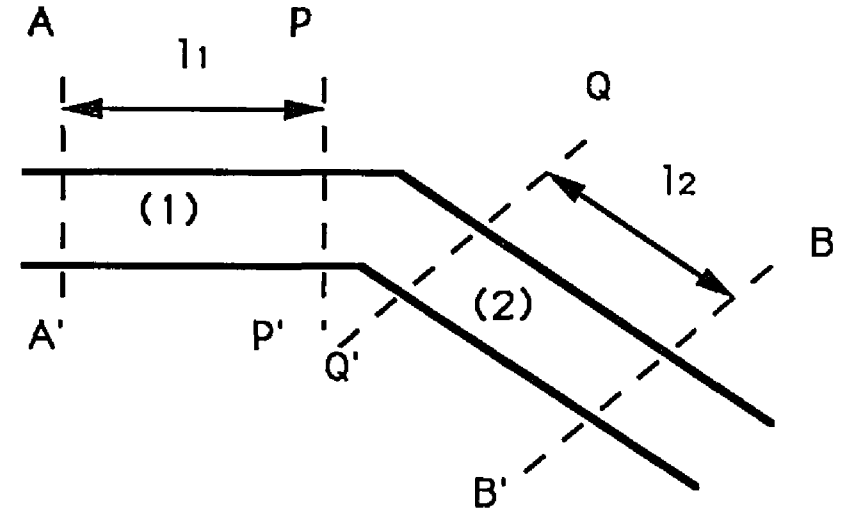

(a)

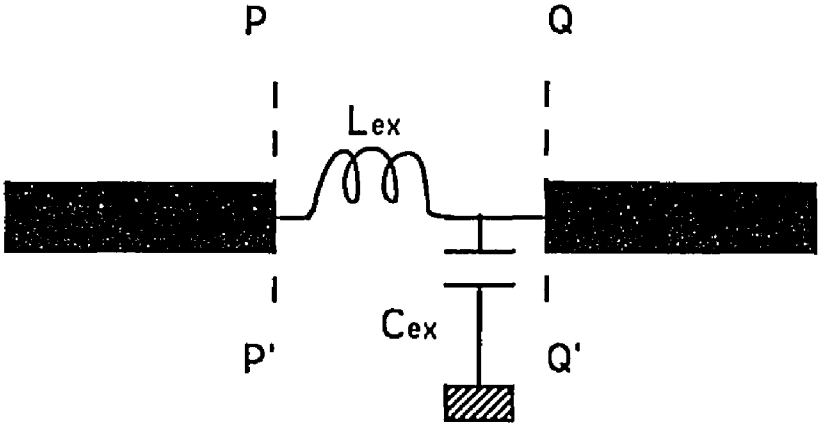

(b)

Figure 4-2 (a) Interconnection conductor with discontinuity; (b) equivalent circuit representation.

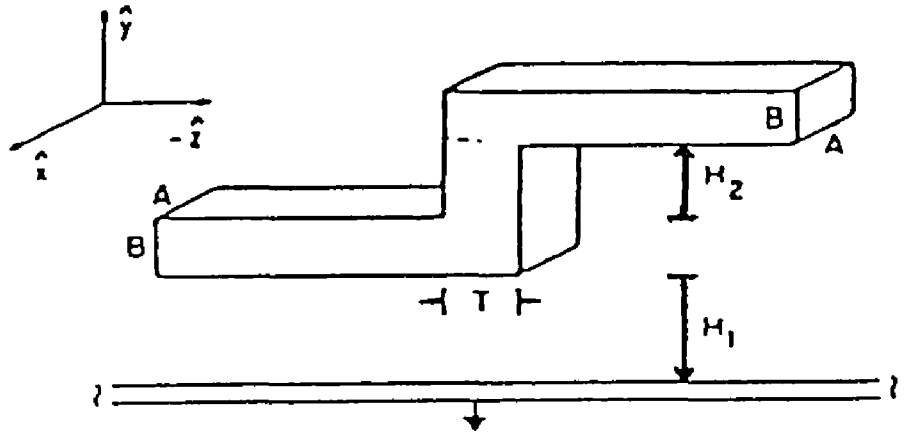

(a)

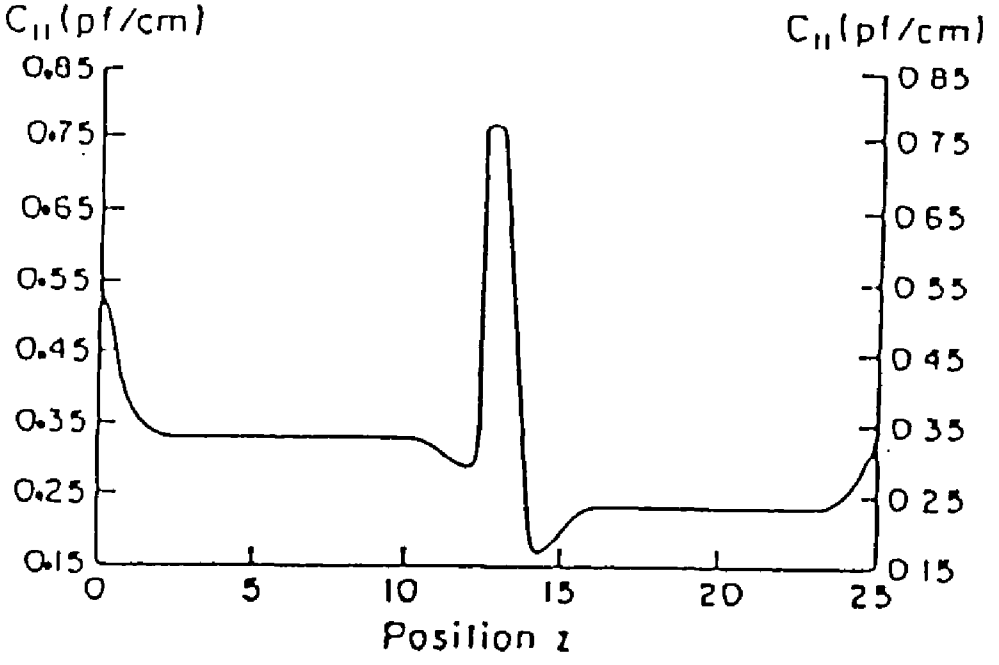

(b)

Figure 4-3 Structure depicting via connection; (a) geometry, (b) p.u.l capacitance.

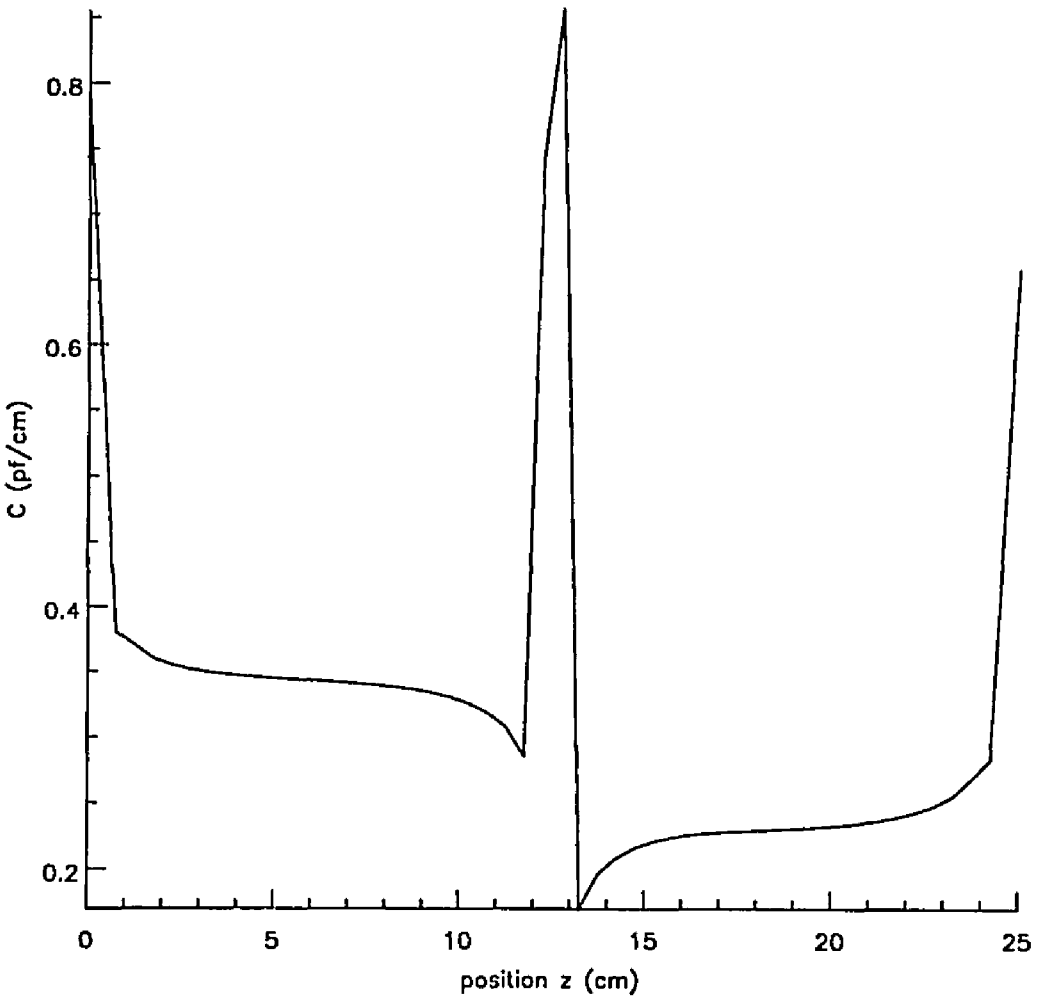

Figure 4-4 The p.u.l. capacitance of a via connection to compare to Figure 4–3b.

On the other hand, when the vertical via is located between semi-infinite strips and all the other dimensions are left unchanged we found that C_{ex}=0.31613pf. This difference is due to the contribution of the charge at the ends of the lines to the total capacitance. This illustrates why it is necessary to use semi-infinite transmission lines if an accurate representation of the capacitance associated with the discontinuity is to be obtained.

4.2.2 A stipline bend

The stripline bend shown in Figure 4–5 is considered next. To simulate a top ground plane we let ϵ_1=100. With parameters, ϵ_2=9ϵ_0, t=8μm, h=75μm, and w=25μm, C_{ex} is calculated for two cases. For the case when the bend is located between finite length strips, l_1=l_2=0.1mm, we obtained C_{ex}=8.291 $\times$ 10^{-15}f. For the second case, where the bend is between two semi-infinitly long strips, the C_{ex} is found to be 2.8462 $\times$ 10^{-15}f. Again, the explanation for the dramatic difference of the two capacitances is the contributions of the ends to the total capacitance for the finite length strip case. Therefore, infinitely long lines (or very long lines) are necessary to reduce this effect.

4.2.3 Coupled microstrip bends

In another example, we calculate the capacitance matrix of two coupled microstrip bends. The geometry is shown on Figure 4–6a. These bends are located between semi-infinite long strips. The strips are located above a substrate with permittivity of 4ϵ_0 and thickness of 25μm. The thickness and width of each strip is the same as the bend discussed above, i.e. t=8μm and w=25μm. The separation

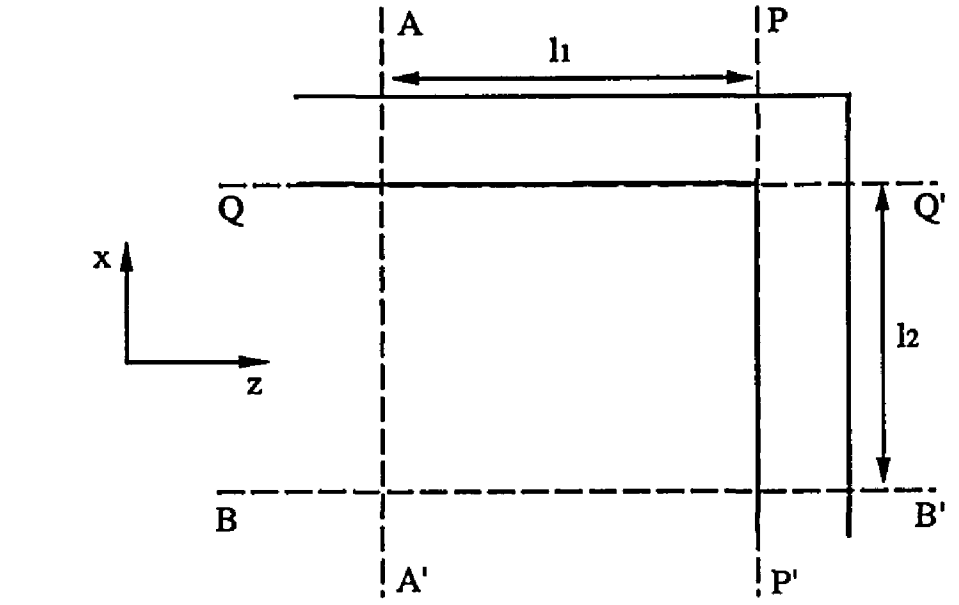

(a)

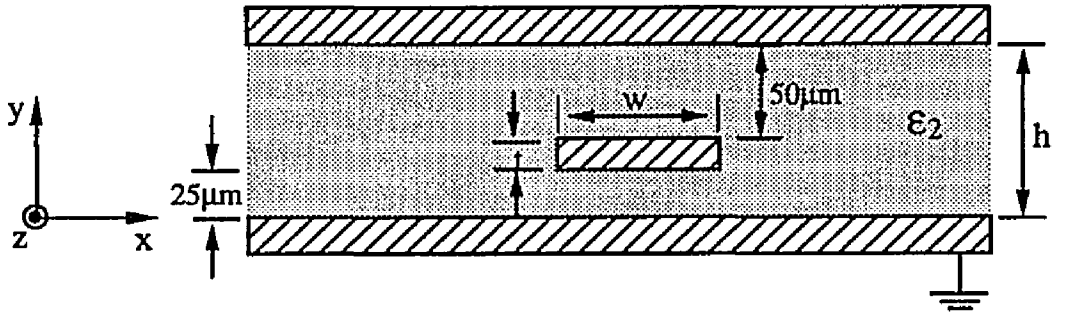

(b)

Figure 4-5 Stripline bend; (a) top view of the bend, (b) cross-sectional view of the stripline.

between the two bends is 25μm. From the 3-D capacitance calculator, we obtain the total capacitance matrix, $C_{T_{11}}$=1.89 $\times$ 10^{-14}f, $C_{T_{12}}$=$C_{T_{21}}$=$-$2.91 $\times$ 10^{-15}f, and $C_{T_{22}}$=2.67 $\times$ 10^{-14}f. We note that the cross sectional views at AA' and at BB' are identical, thus resulting identical p.u.l. capacitance matrix. From the 2-D capacitance calculator, we obtain a p.u.l. capacitance matrix of $C_{pul_{11}}$=$C_{pul_{22}}$=8.31 $\times$ 10^{-11}f/m, and $C_{pul_{12}}$=$C_{pul_{21}}$=$-$1.08 $\times$ 10^{-}15f. Then, applying (4.1) for each element of the capacitance matrix, the following excess capacitance matrix is obtained, C_{11}=2.64 $\times$ 10^{-15}f, C_{12} = C_{21}=$-$7.50 $\times$ 10^{-16}f, and C_{22}=1.04 $\times$ 10^{-14}f. Figure 4–7 shows the equivalent circuit representation.

4.2.4 Coupled double-bend microstrips

Here, interconnections with bends other than 90 degrees are considered. A top view of the geometry under consideration is shown in Figure 4–8a, while a cross sectional view is shown in Figure 4–8b. Each interconnection consists of three uniform sections; two semi-infinite strips and one connecting transition strip at a 45 degree slope. Since the middle section of each interconnection is a short transition, it considered as a discontinuity; and therefore, is represented by lumped elements. If the transition was gradual and long then we would have modeled it as a non-uniform transmission-line and characterized it by its p.u.l. capacitance and inductance. An equivalent circuit representation is given in Figure 4–7, where C_{11}=C_{22}=0.01pf and C_{12}=C_{21}=-0.003pf. These results were obtained in a similar fashion to those of the previous example.

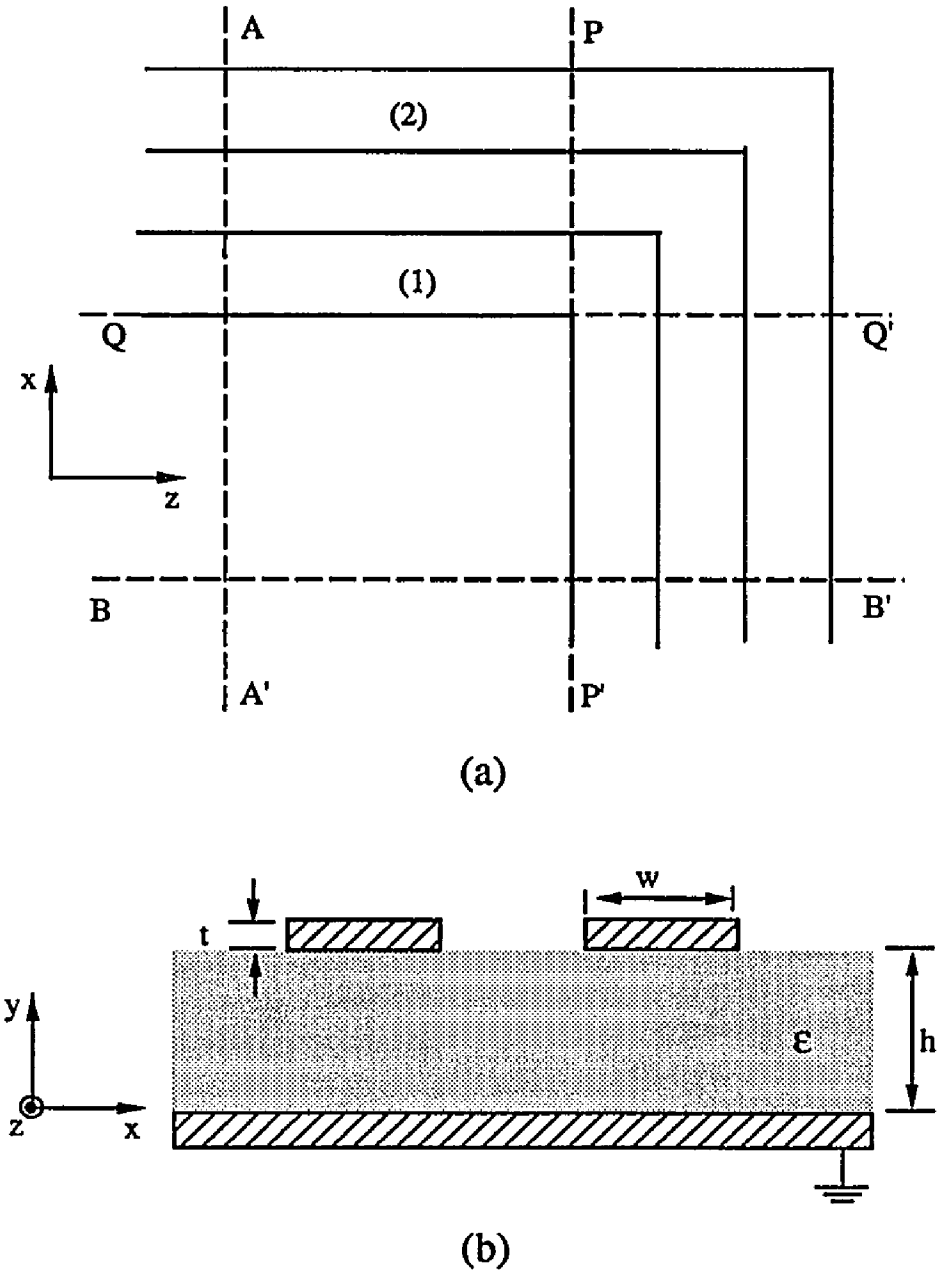

Figure 4-6 Microstrip bends; (a) top view of the bends, (b) cross-sectional view of the microstrips.

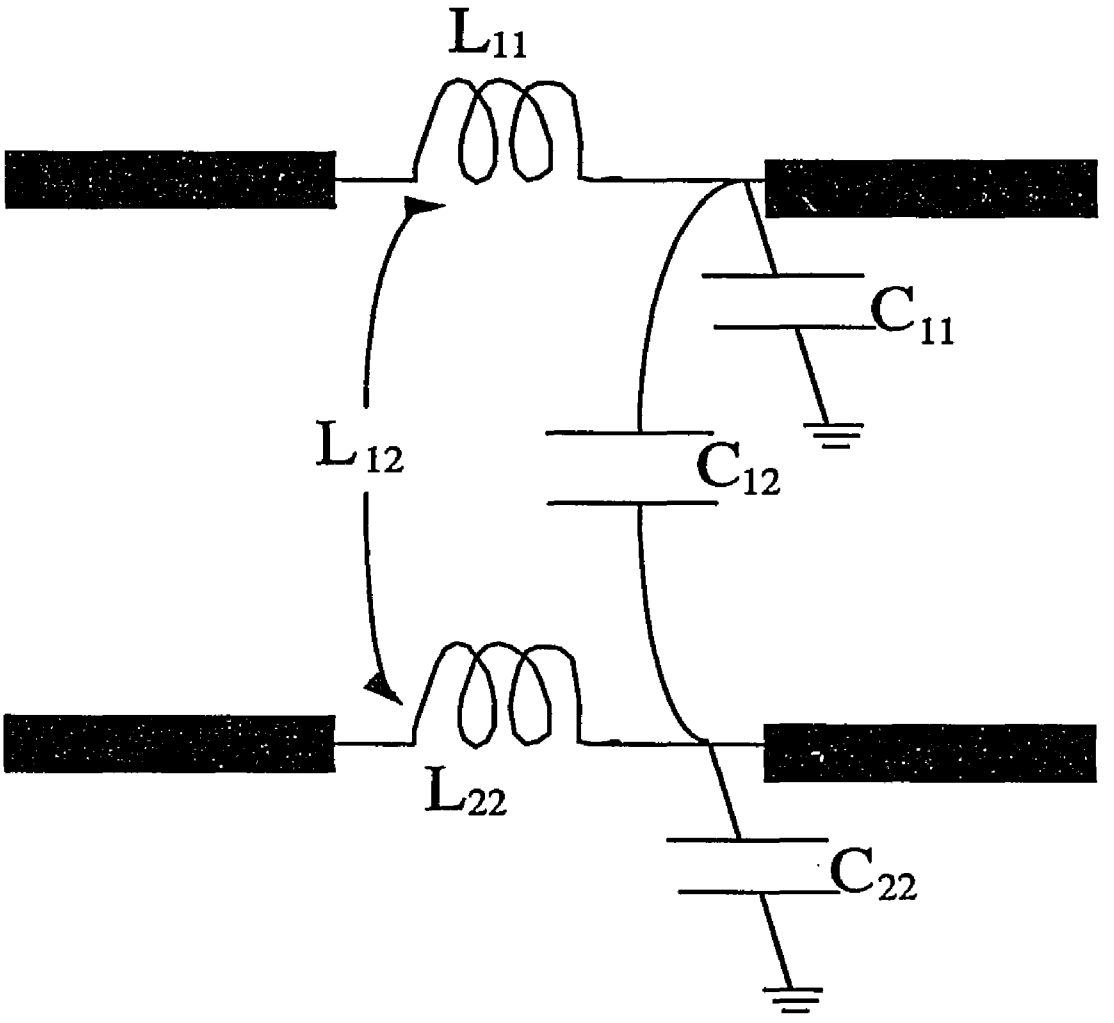

Figure 4-7 Equivalent circuit representation of two coupled interconnections with discontinuities.

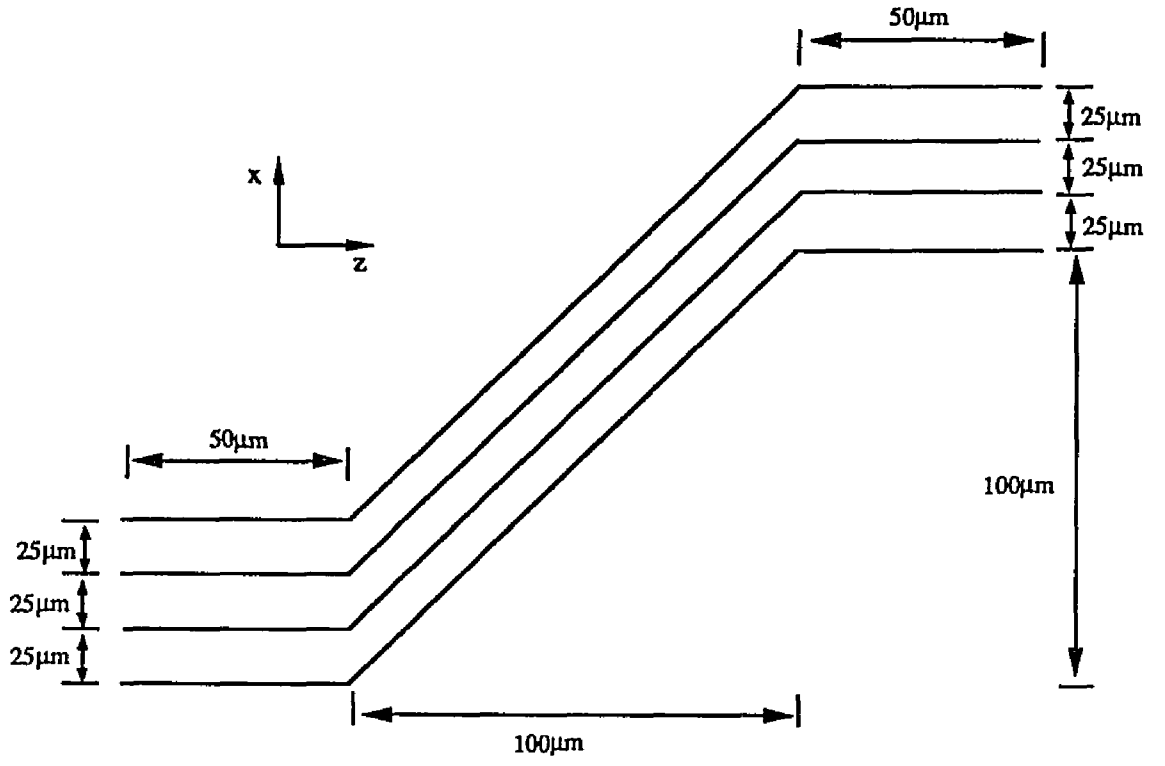

(a)

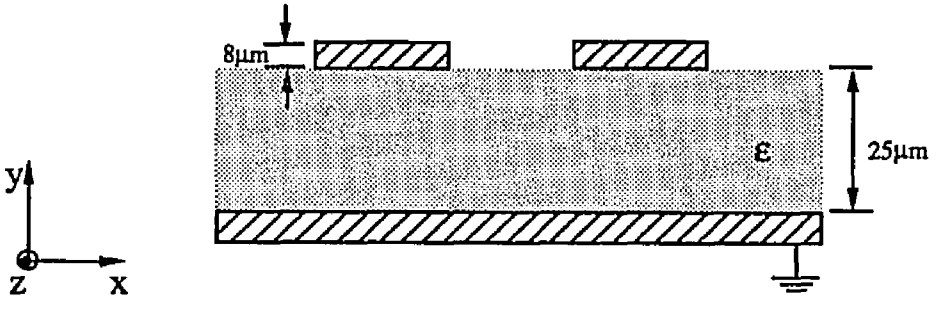

(b)

Figure 4-8 Coupled double-bend microstips; (a) top view of the strips, (b) cross-sectional view of the microstrips.

4.2.5 Cross-over stripline

In this section, cross-over stripline is considered. In particular, the effect of the separation d between the conductors and the width w of conductors on the excess capacitance is investigated. The geometry under consideration is shown in Figure 4–9. We consider the case were the separation between the ground planes is 50μm and the relative dielectric permittivity is 5. Moreover, the separation between one ground plane and the active conductor is fixed at 12μm. A graph of C_{ex} as a function of w and d is shown in Figure 4–10. This graph shows that C_{ex} is more sensitive to changes in d than changes in w. This is expected since a change in d more strongly effects the electric fields between the cross-over conductors and the ground planes.

4.3 The P.U.L. Capacitance of Flaring Microstrip Lines

Flaring interconnections appear commonly in high speed VLSI packages. Under TEM assumptions, their transmission-line representation is based on position dependent p.u.l capacitance and inductance, $C(z)$ and $L(z)$, obtained using two-dimensional parameter extractors. To assess the accuracy of this approach and its limitations, it is necessary to study the three-dimentional problem.

4.3.1 Coupled flaring lines of finite length

First, the geometry of two coupled, flaring microstrip lines is considered. Figure 4–11a shows the top view of the geometry, while Figure 4–11b shows its variable cross section. The thickness of each strip was 8μm. The thickness of the substrate was h=25μm and its permittivity ϵ_2=4ϵ_0. The upper dielectric medium

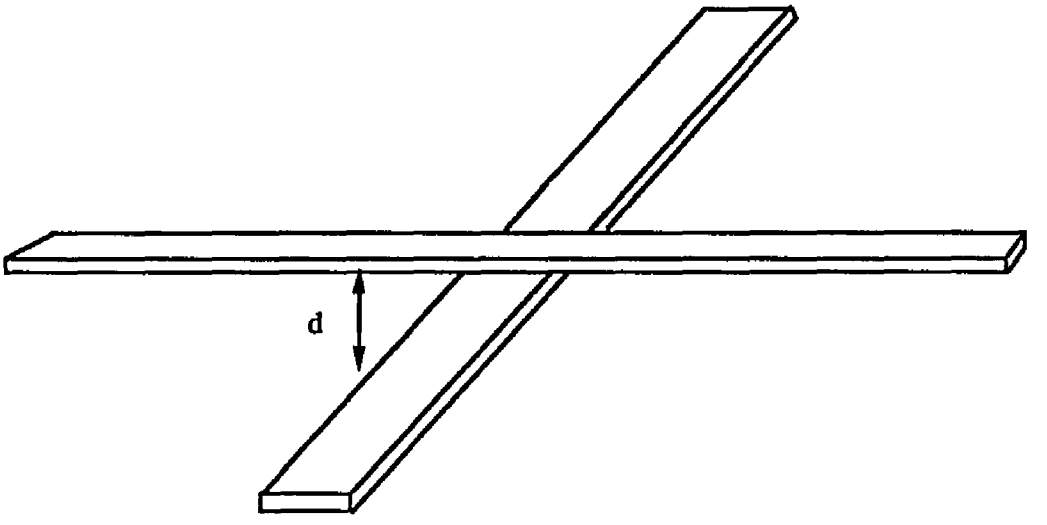

(a)

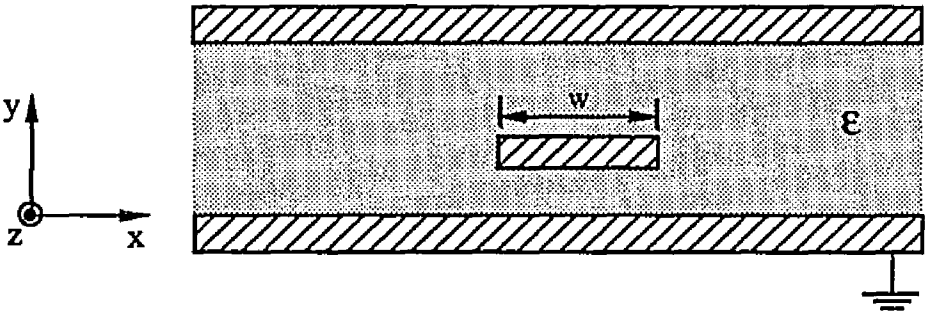

(b)

Figure 4-9 Geometry of a cross-over.

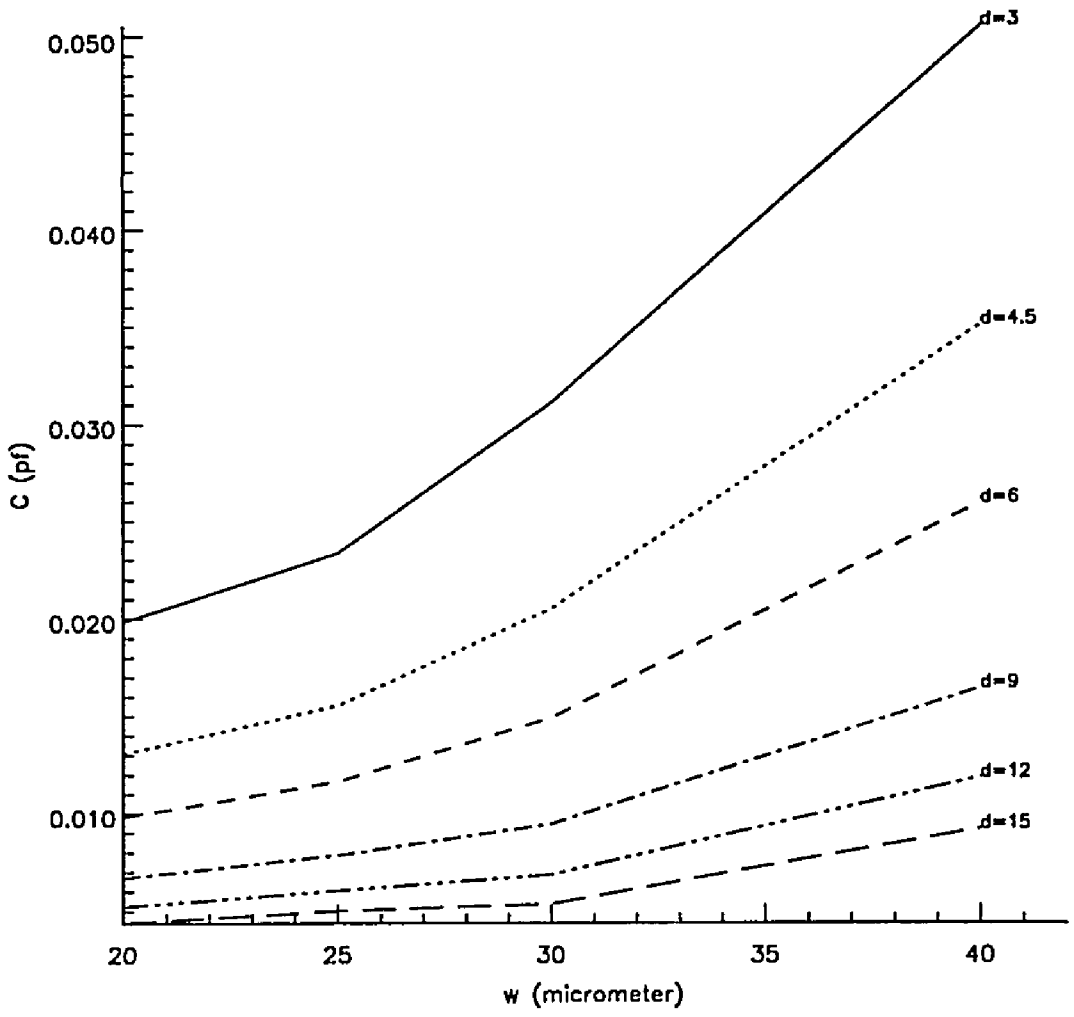

Figure 4-10 Excess capacitance for cross-over stripline vs. width and separation.

was air with $\epsilon_1=\epsilon_0$. The solid curve in Figure 4–12 shows the p.u.l. capacitances C_{11} and C_{22} for the two lines. The fact that the two are indistinct is due to the very smooth variation of the cross section from one end of the line to the other. Indeed, the two conductors start with the same width w=25μm, and undergo a change of width by a factor of two over a distance equal to forty times their initial width. The edge effect is apparent, resulting in an increased value of the p.u.l. capacitance at the two ends of the conductors. The variation of the mutual capacitance is depicted by the solid curve in Figure 4–13.

The dotted curves in Figures 4–12 and 4–13 depict the p.u.l. self and mutual capacitances, respectively, obtained using a two-dimensional capacitance calculator in the following manner. The end values (at 0.0mm and 1.0mm) correspond to the self and mutual capacitances for the coupled microstrip lines of infinite extent with cross sections identical to the end cross sections of the non-uniform geometry. Then, the per-unit-length variation is obtained by interpolating between these end values. This corresponds to a very fine approximation of the non-uniform structure by a large number of uniform transmission line sections. While the values for the mutual capacitance predicted by the two approaches are in very good agreement, the two-dimensional approximation underestimates the value of the self capacitance. Undoubtedly, the two-dimensional result is dependent on the way the non-uniform structure is approximated. For example, instead of using cross sections parallel to the end planes of the non-uniform structure, cross sections could be defined by planes perpendicular to an effective interconnect axis qq' as shown in Figure 11a. For very smooth structures, such different choices in the uniform-section approximation of the interconnection are expected to lead to almost identical results. However, if the non-uniformity of the structure is significant, the p.u.l. capacitances

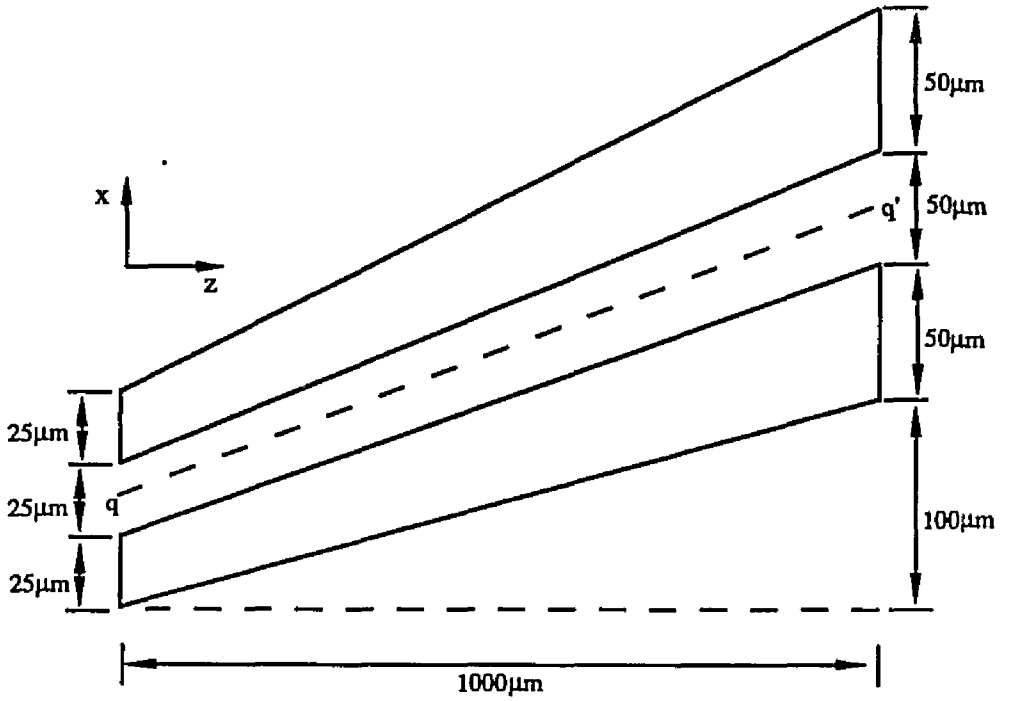

(a)

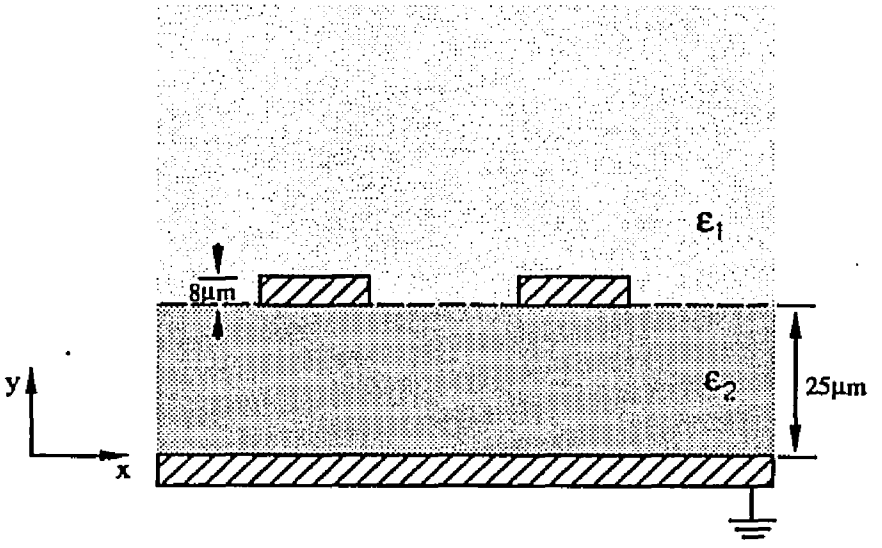

(b)

Figure 4-11 The geometry of flaring coupled microstrip line of finite extent. (a) top view; (b) cross section.

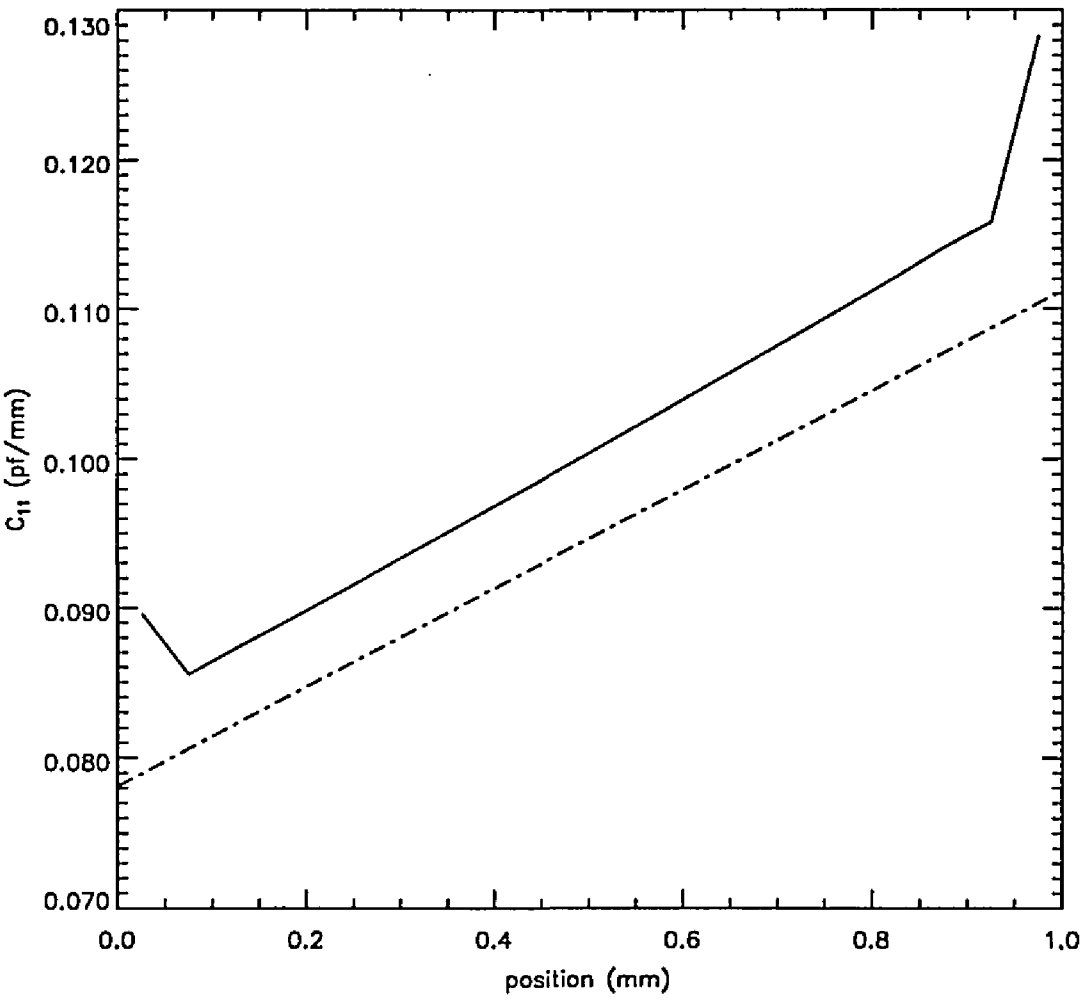

Figure 4-12 The p.u.l. self-capacitance ($C_{11} = C_{22}$) for the geometry of Figure 4–11.

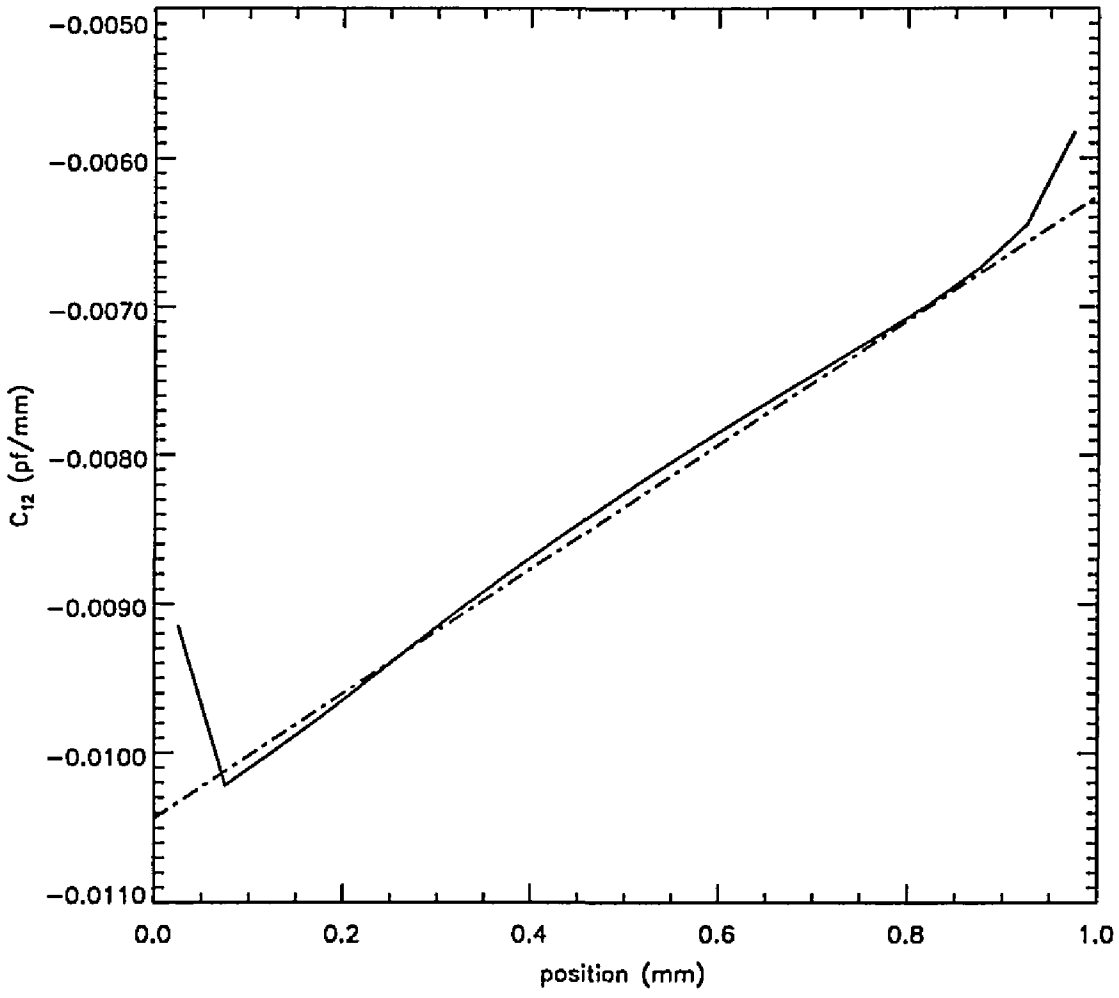

Figure 4-13 The p.u.l. mutual capacitance ($C_{12} = C_{21}$) for the geometry of Figure 4–11.

predicted by the different uniform-section approximations may differ considerably. In such cases, the three-dimensional modeling comes to the rescue since the total capacitance is calculated accurately, and thus an accurate prediction of the overall signal delay is ensured.

4.3.2 A flaring transition between two semi-infinite strips

Next, a single microstrip interconnection is considered. The interconnection consists of a flaring transition between two semi-infinite strips with thickness of 8μm as shown in Figure 4–14a. Its variable cross section is shown in Figure 4–14b. The thickness of the substrate was h=25μm and its permittivity $\epsilon_2 = 4\epsilon_0$. The upper dielectric medium was air with $\epsilon_1 = \epsilon_0$. A plot of the p.u.l. capacitance in the z direction of this structure is given in Figure 4–15. As expected the p.u.l capacitance of the uniform sections is constant. Moreover, the p.u.l. capacitance of the flaring section increases as the width of the conductor increases. It is very intresting to observe how this plot resembles the structure itself.

The impedance of this structure gradually decreases from about 70Ω at z=0 to 25Ω at z=1875μm. It is worthwhile to examine how many discrete sections of constant impedences, $(Z_1, Z_2, \cdots, Z_N)$, is required to approximate the exact continuous position dependent impedence $Z(z)$ (see Figure 16). The number of discrete sections can be obtained by comparing the exact reflection coefficient Γ with the approximate one Γ_N. The exact reflection coefficient is calculated from the following [Pozar, 1990]

$$\Gamma(f) = \frac{1}{2}\int_0^L \exp\left(-j2\frac{2\pi L}{\lambda_g}\right)\frac{d}{dz}\ln\left(\frac{Z(z)}{Z_0}\right)dz \qquad (4.3)$$

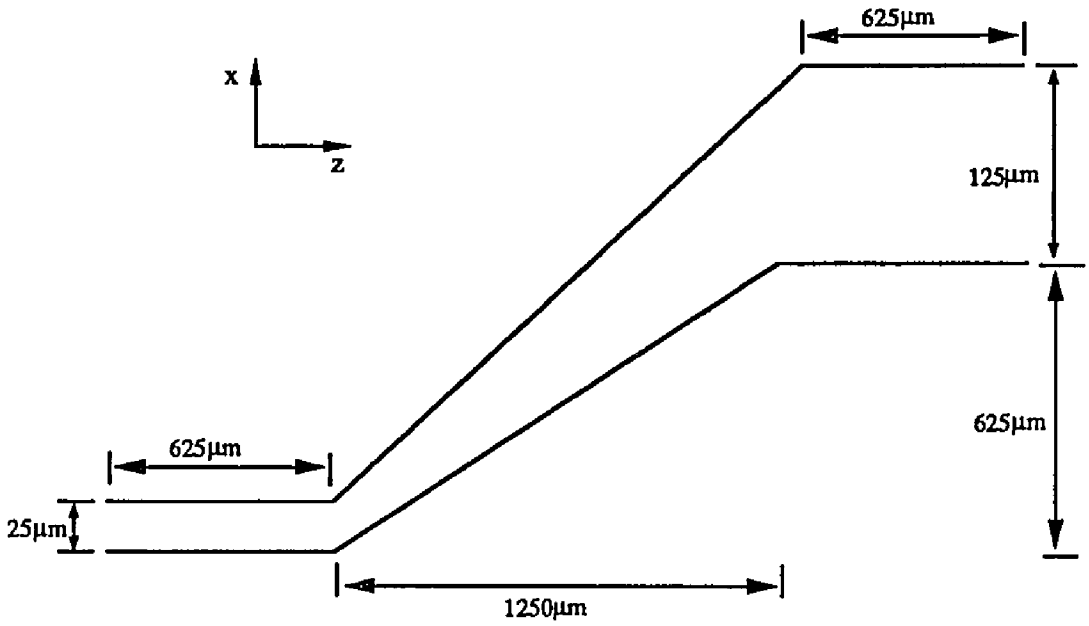

(a)

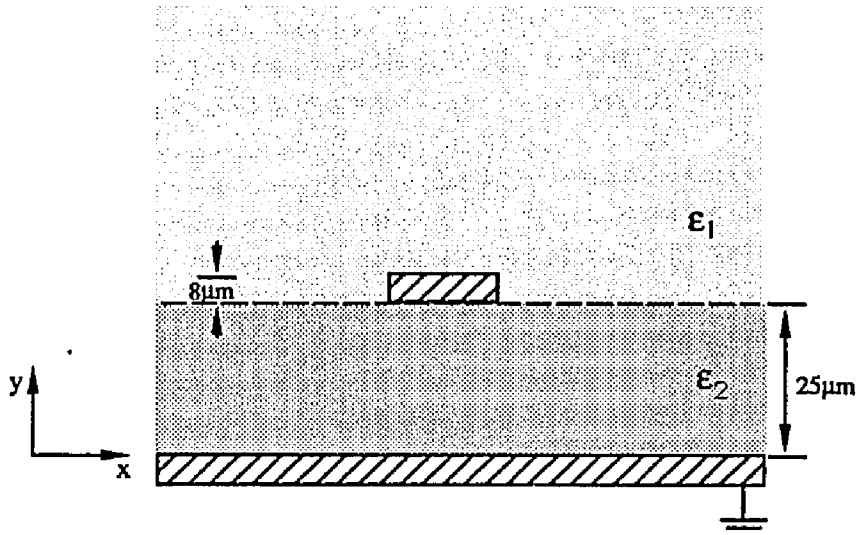

(b)

Figure 4-14 The geometry of a flaring microstrip line of infinite extent. (a) top view; (b) cross section.

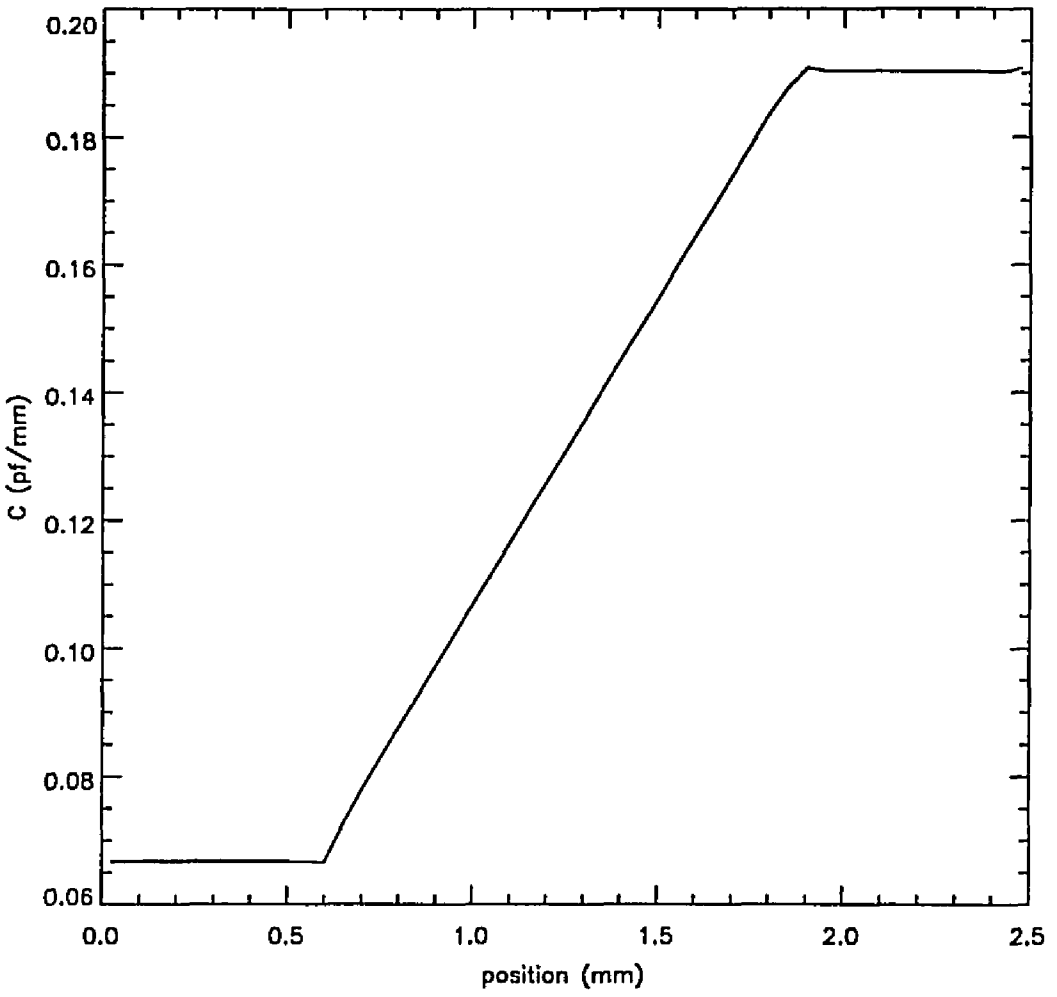

Figure 4-15 The p.u.l. capacitance for the geometry of Figure 4–14.

where λ_g is the guide wavelength. For microstrip, $\lambda_g = c/(f\sqrt{\epsilon_{eff}})$. Figure 17 shows a comparison of the two. Notice that 6 sections result in an acceptable approximation.

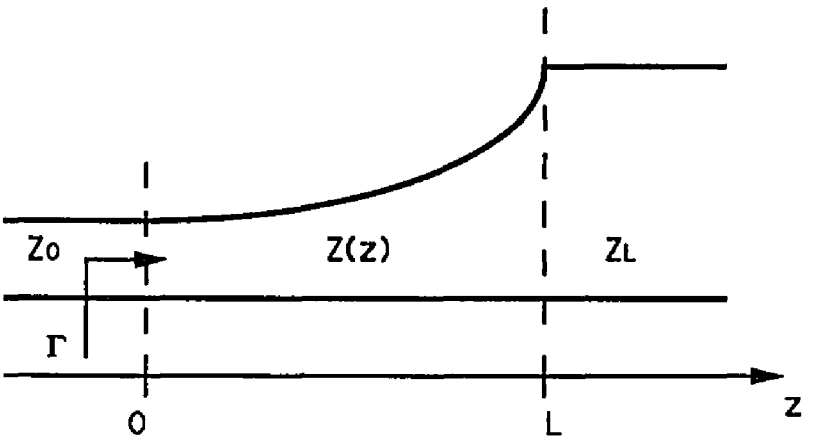

(a)

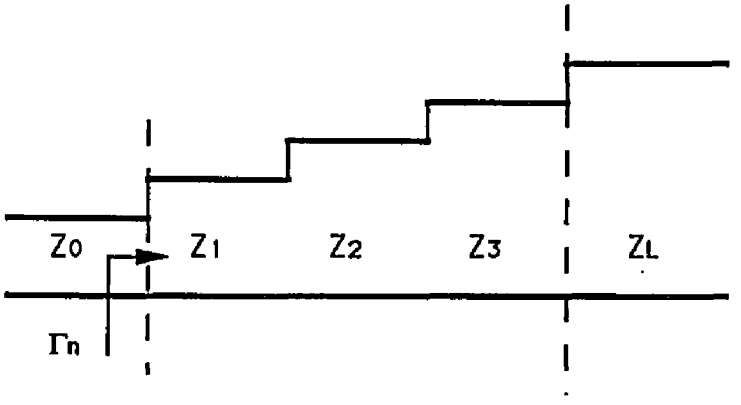

(b)

Figure 4-16 Discritizing $Z(z)$ for waveform simulation; (a) exact $Z(z)$, (b) approximating discrete Z_i's.

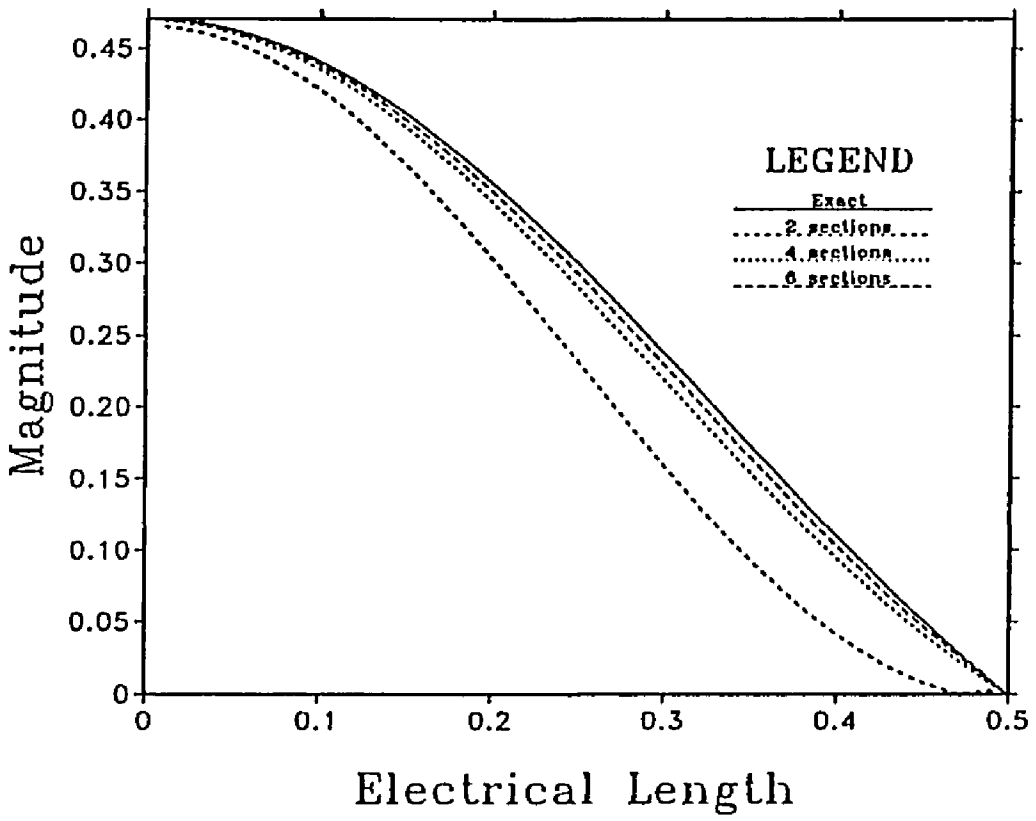

Figure 4-17 The reflection coefficient vs. electrical length.

CHAPTER 5

CONCLUSIONS

A three-dimensional capacitance calculator, based on an integral equation formulation for the electrostatic charge distribution on the conductors, has been developed. The primary objective was to develop a computer program for the calculation of the capacitance matrix and/or the p.u.l. capacitance matrix of frequently used structures in today's VLSI packaging interconnections. Operating under quasi-TEM conditions, the program can be used to extract capacitive elements used in the lumped equivalent circuit representations of interconnection discontiniuties.

The mathematical formulation uses Green's functions pertinent to single-substrate microstrip, homogeneous stripline geometries and strip conductors embedded in a homogenous medium above ground plane. For these geometries, the p.u.l. inductance matrix can be obtained in a straightforward manner by means discussed in chapter 2. For three-dimensional computations, finite-length line Green's functions have been used in order to reduce the two-dimensional integrals to one-dimensional integrals. Thus, computer labor is significantly reduced. When infinitely long conductors are encountered, a two-dimensional capacitance calculator is utilized for the uniform sections away from any discontinuities. Consequently, both computer memory and time are saved. In this case, Green's functions for semi-infinite lines are required in order to include the results of the two dimensional calculator into the overall formulation. All the above mentioned Green's functions are appropriatly chosen to satisfy the boundary conditions at the dielectric interfaces and the infinite ground plane in order to minimize the number of unknowns.

An appropriate discretization scheme, for best approximation, has been proposed. In this scheme, all non-rectangular discrete elements are approximated with the best fitting rectangular. In addition, it has been shown that this approximation is adequate for the conductor geometries under consideration. The method of moments is used for the numerical approximation and solution of the integral equation.

Several applications of the computer program have been presented. The validity of this program was tested by calculating the capacitance of finite-length, uniform conductors of rectangular cross sections and comparing the results with others available in the literature and obtained by other means. Also, the p.u.l. capacitance and the excess capacitance of a vertical via was presented. The lumped capacitive element matrix was obtained for a stripline bend, two coupled microstrip bends, a stripline cross-over, and coupled double bend microstrips. The equivelent circuit representation of these geometries was also presented. Numerical results for the capacitance matrix of a flaring, coupled microstrip geometry of finite length have been presented and comparisons have been made with results obtained using an approximate model of the structure created by cascading uniform sections of coupled transmission lines. The cross-sectional dimensions of each of these uniform sections are obtained on the basis of its position along the non-uniform line under study, and its capacitance matrix is calculated using a two-dimensional program. The use of the rigorous three-dimensional capacitance extractor presented here becomes essential for those non-uniform structures where different segmentation schemes lead to significant discrepancies in the calculated p.u.l. capacitance matrices. It is important to notice that for interconnection discontinuities such as bends and vias, or short nonuniform transitions like the twice-bent microstrips, the best modeling is

to use the lumped circuit representation. While uniform lines and long nonuniform lines are best characterized by the p.u.l. capacitance and p.u.l inductance.

The applications and examples provided in this work were chosen to illustrate some of the issues involved in the analysis of VLSI packaging interconnections. However, there are other issues that need to be investigated in the future. For example, an investigation should be carried out to determine how far away form a discontinuity one needs to be before a uniform charge distribution can be assumed. Ideally, one could relate this distance to the physical parameters of the structure. Also, studies can carried out to determine how the capacitance depends on the various parameters, such as the angle between crossover conductors and the angle of a bend. Other applications may include coupling effects of multiple discontinuities.

APPENDIX A

DERIVATION OF THE GREEN'S FUNCTIONS

The derivation of the Green's functions used in the formulation of the integral equations is given in this Appendix. First, we derive expressions for a point charge, and then obtain the proper expressions for the line charges. The following is a revision of derivation carried out by Mechiak, [1989].

Consider the two layer media above a ground plane of infinite extent as shown in Figure 2–2 (other conductors excluded). Let V be an open bounded region in three-dimensional space and let S be its boundaries. Imagine a point charge of unit magnitude located at some point (x', y', z') in V. Then, the Green's function $G(\mathbf{r}, \mathbf{r}')$ is the electrostatic potential at some other point (x, y, z) due to the unit point source. This Green's function is the solution to the Poisson's equation

$$\nabla \cdot \left(\epsilon(\mathbf{r}) \nabla G(\mathbf{r}, \mathbf{r}')\right) = -\delta(\mathbf{r} - \mathbf{r}') \tag{A.1}$$

subject to the following boundary conditions

$$G(\mathbf{r}, \mathbf{r}')\Big|_{y=h^+} = G(\mathbf{r}, \mathbf{r}')\Big|_{y=h^-} \tag{A.2a}$$

$$\epsilon_1 \frac{\partial G}{\partial y}\Big|_{y=h^+} = \epsilon_2 \frac{\partial G}{\partial y}\Big|_{y=h^-} \tag{A.2b}$$

$$G(\mathbf{r}, \mathbf{r}')\Big|_{y=0} = 0 \tag{A.3a}$$

$$\lim_{\mathbf{r} \to \infty} G(\mathbf{r}, \mathbf{r}') = 0 \tag{A.3b}$$

where $r^2 = x^2 + y^2 + z^2$ and $r'^2 = x'^2 + y'^2 + z'^2$.

The solution of (A.1) can be written as a superposition of the primary potential G^p and a secondary potential G^s which is due to the induced charges at the interface and the ground plane [Wait,1985]. Thus,

$$G = G^p + G^s \tag{A.4}$$

It is well known that

$$G^p = \frac{1}{4\pi\epsilon|\mathbf{r}-\mathbf{r}'|} \tag{A.5a}$$

or in cylindrical coordinates

$$G^p = \frac{1}{4\pi\epsilon\sqrt{\varrho^2+\Delta y^2}} \tag{A.5b}$$

where $\varrho^2 = \Delta x^2 + \Delta z^2$, $\Delta x = x - x'$, $\Delta z = z - z'$, and $\Delta y = y - y'$. Using Weber's Integral we can rewrite (A.5b) as

$$G^p = \frac{1}{4\pi\epsilon}\int_0^\infty J_0(\lambda\varrho)e^{-\lambda|y-y'|}d\lambda \tag{A.5c}$$

where J_0 is Bessel function of first kind and zero order, and the negative sign in the exponential is chosen so that (A.3b) is satisfied. Likewise, G^s can be expressed in terms of similar integrals. If the source is located in the region *above* the interface (i.e. $y' \geq h$), then the Green's function, G_{aa}, for field points *above* the interface ($y \geq h$) is

$$G_{aa} = \frac{1}{4\pi\epsilon_1}\int_0^\infty \left[e^{-\lambda|y-y'|} + R(\lambda)e^{-\lambda(y-y')}\right] J_0(\lambda\varrho)d\lambda \tag{A.6a}$$

Similarly, the Green's function for the region *below* the interface ($0 \leq y \geq h$) can be written as

$$G_{ab} = \frac{1}{4\pi\epsilon_2}\int_0^\infty \left[A(\lambda)e^{-\lambda y} + B(\lambda)e^{\lambda y}\right] J_0(\lambda\varrho)d\lambda \tag{A.6b}$$

where R, A, and B are unknowns yet to be determined. Application of the boundary conditions at $y = 0$ and $y = h$ leads to the solution of the unknowns

$$R = -\frac{(1 + Ee^{2\lambda h})}{(1 + Ee^{-2\lambda h})} e^{-2\lambda y'} \tag{A.7a}$$

$$A = -B = \frac{-2\epsilon_1}{(\epsilon_1 + \epsilon_2)} \frac{e^{-\lambda y'}}{(1 + Ee^{-2\lambda h})} \tag{A.7b}$$

where $E = \frac{\epsilon_2 - \epsilon_1}{\epsilon_1 + \epsilon_2}$. Since $|Ee^{-2\lambda h}| \leq 1$, we utilize the following series expansion

$$\frac{1}{(1 + Ee^{-2\lambda h})} = \sum_{k=0}^{\infty} (-1)^k E^k e^{-2k\lambda h} \tag{A.8}$$

After substituting (A.7a,b) and (A.8) into (A.6a,b), the resulting integrals can be evaluated using (A.5c). After algebric manupilations we obtain

$$G_{aa} = \frac{1}{4\pi\epsilon_1} \left[\frac{1}{\sqrt{\Delta x^2 + \Delta z^2 + \Delta y^2}} - \frac{1}{\sqrt{\Delta x^2 + \Delta z^2 + (y + y')^2}} + \sum_{k=1}^{\infty} (-1)^k E^k \right.$$
$$\left. \left\{ \frac{1}{\sqrt{\Delta x^2 + \Delta z^2 + (y + y' + 2(k-2)h)^2}} - \frac{1}{\sqrt{\Delta x^2 + \Delta z^2 + (y + y' + 2kh)^2}} \right\} \right] \tag{A.9}$$

$$G_{ab} = \frac{1}{2\pi(\epsilon_1 + \epsilon_2)} \sum_{k=0}^{\infty} (-1)^k E^k \left[\frac{1}{\sqrt{\Delta x^2 + \Delta z^2 + (y - y' - 2kh)^2}} \right.$$
$$\left. - \frac{1}{\sqrt{\Delta x^2 + \Delta z^2 + (y + y' + 2kh)^2}} \right] \tag{A.10}$$

Following a formulation similar to the above one, the Green's functions due to a point charge which is located *below* the interface can be obtained. For $y \geq h$

the function is denoted by G_{ba}, and for $y \leq h$, it is denoted by G_{bb}. The expressions for these Green's functions are found to be

$$G_{ba} = \frac{1}{2\pi(\epsilon_1+\epsilon_2)} \sum_{k=0}^{\infty} (-1)^k E^k \left[\frac{1}{\sqrt{\Delta x^2 + \Delta z^2 + (y - y' + 2kh)^2}} - \frac{1}{\sqrt{\Delta x^2 + \Delta z^2 + (y + y' + 2kh)^2}} \right] \tag{A.11}$$

$$G_{bb} = \frac{1}{4\pi\epsilon_2} \left[\frac{1}{\sqrt{\Delta x^2 + \Delta z^2 + \Delta y^2}} - \frac{1}{\sqrt{\Delta x^2 + \Delta z^2 + (y + y')^2}} + \sum_{k=1}^{\infty} (-1)^k E^k \left\{ \frac{1}{\sqrt{\Delta x^2 + \Delta z^2 + (y - y' + 2kh)^2}} - \frac{1}{\sqrt{\Delta x^2 + \Delta z^2 + (y + y' + 2kh)^2}} + \frac{1}{\sqrt{\Delta x^2 + \Delta z^2 + (y - y' - 2kh)^2}} - \frac{1}{\sqrt{\Delta x^2 + \Delta z^2 + (y + y' - 2kh)^2}} \right\} \right] \tag{A.12}$$

After obtaining the Green's functions for a point charge, we are then able to obtain expressions for the Green's functions of line charges. First, let us find the Green's function for a finite length line charge that extends from z_1 to z_2 and is located at (x', y'). Let G^{3d} denote this Green's function.

$$G^{3d} = \int_{z_1}^{z_2} G(\mathbf{r}, \mathbf{r}') dz' \tag{A.13}$$

We note that all the previous Green's functions for the point charge involve expressions of the form $\frac{1}{\sqrt{\Delta z^2 + c}}$; thus, let us consider the integration of this generic

expression. Here, the positive root of the square root is chosen.

$$\begin{aligned} I &= \int_{z_1}^{z_2} \frac{dz'}{\sqrt{\Delta z^2 + c}} \\ &= \int_{z_1}^{z_2} \frac{dz'}{\sqrt{|z - z'|^2 + c}} \end{aligned} \tag{A.14}$$

where we have assumed that $z_1 < z_2$. Let $\Delta z_1 = z_1 - z$ and $\Delta z_2 = z_2 - z$. There are three cases to consider when evaluating this integral. When $z < z_1$, we obtain

$$I = \ln \frac{\Delta z_2 + \sqrt{\Delta z_2{}^2 + c}}{\Delta z_1 + \sqrt{\Delta z_1{}^2 + c}} \tag{A.15a}$$

In the case where $z_1 < z < z_2$, I is evaluated to be

$$I = \ln \frac{(\Delta z_2 + \sqrt{\Delta z_2{}^2 + c})(-\Delta z_1 + \sqrt{\Delta z_1{}^2 + c})}{c} \tag{A.15b}$$

Finally, when $z > z_2$, we have

$$I = \ln \frac{-\Delta z_1 + \sqrt{\Delta z_1{}^2 + c}}{-\Delta z_2 + \sqrt{\Delta z_2{}^2 + c}} \tag{A.15c}$$

Actually, all the above expressions for I can be shown to be the same, except when $c = 0$. Substituting the appropriate value of c in the expressions in (A.9) through (A.12), we obtain (2.30) through (2.33) where we used the expression in (A.15a). However, one must be careful about the case c approaches zero when carrying out any calculations.

Next, we consider the cases of the semi-infinite lines. When $z_1 \to -\infty$, (A.15c) is the appropriate form to use. We notice that the functions for the finite lines consist of expressions of the form

$$I_F = \ln \frac{F_{11}}{F_{21}} \frac{F_{22}}{F_{12}} \tag{A.16a}$$

where

$$F_{11} = -\Delta z_1 + \sqrt{\Delta z_1{}^2 + c_1} \tag{A.16b}$$

$$F_{12} = -\Delta z_1 + \sqrt{\Delta z_1{}^2 + c_2} \tag{A.16c}$$

$$F_{21} = -\Delta z_2 + \sqrt{\Delta z_2{}^2 + c_1} \tag{A.16e}$$

$$F_{22} = -\Delta z_2 + \sqrt{\Delta z_2{}^2 + c_2} \tag{A.16f}$$

As z_1 becomes a large negative number, both F_{11} and F_{12} become very large and cancel out. Thus,

$$\lim_{z_1 \to -\infty} I_F = \ln \frac{F_{22}}{F_{21}} \tag{A.17}$$

Using this evaluation for all the terms of G^{3d}, we obtain the results for $G^{-\infty}$ given by (2.35) through (2.38). Understandably, the expressions for $G^{+\infty}$ are obtained in an analagous manner. Letting $z_2 \to +\infty$ and utilizing the form in (A.15a), we obtain the results given in (2.40) through (2.43).

Lastly, we consider the case of an infinitely long line. Since $z_1 \to -\infty$ and $z_2 \to +\infty$, (A.15b) must be used. Then

$$I_F = \ln \frac{F_{21} F_{11}}{c_1} \frac{c_2}{F_{12} F_{22}} \tag{A.18a}$$

where

$$F_{11} = -\Delta z_1 + \sqrt{\Delta z_1{}^2 + c_1} \tag{A.18b}$$

$$F_{12} = -\Delta z_1 + \sqrt{\Delta z_1{}^2 + c_2} \tag{A.18c}$$

$$F_{21} = \Delta z_2 + \sqrt{\Delta z_2{}^2 + c_1} \tag{A.18e}$$

$$F_{22} = \Delta z_2 + \sqrt{\Delta z_2{}^2 + c_2} \tag{A.18f}$$

As $z_1 \to -\infty$ and $z_2 \to +\infty$, F_{11} and F_{12} cancell out as do F_{21} and F_{22}.

$$\lim_{\substack{z_1 \to -\infty \\ z_2 \to +\infty}} I_F = \ln \frac{c_2}{c_1} \tag{A.19}$$

The results obtained for G^{2d} are given by (2.45) through (2.48).

REFERENCES

Abramowitz, M. and I.A. Stegun (1972), Handbook of Mathematical Functions, Dover, New York, pp. 916-919.

Becker, E.B., G.F. Carey, and J.T. Oden (1981), Finite Elements; An Introduction, vol. 1, Prentice-Hall, New Jersey.

Cangellaris, A.C., J.L.Prince, and L.P.Vakanas (1990), "Frequency-Dependent Inductance and Resistance Calculation for Three-Dimensional Structures in High-Speed Interconnect Systems," IEEE Trans. Comp.,Hyprids, Munf. Technol., CHMT-13(1), pp. 893-897.

Carin, L. and K.J. Webb (1989), "Multiconductor Transmission Lines in Multiple Dielectric Media," IEEE Trans. Microwave Theory Tech., MTT-37(11), pp. 1784-1793.

Haberman, R. (1987), Elementry Applied Partial Differential Equations, Prentice-Hall, New Jersey.

Harrington, R.F. (1968), Field Computation by Moment Methods, MacMillan, New York.

Harrington, R.F. (1961), Time-Harmonic Electromagnetic Fields, McGraw-Hill, New York.

Huebner, K.H. (1975), The Finite Element Method for Engineers, John Wiley and Sons, New York , pp. 143-145.

Lindell, I.V. and Q. Gu (1987), "Theory of time-domain quasi-TEM modes in inhomogeneous multiconductor lines," IEEE Trans. Microwave Theory Tech., MTT-35(10), pp. 893-897.

Mechaik, M.M. (1989), Private comminucations.

Palusinski, O.A. and A. Lee (1989), "Analysis of transients in nonuniform and uniform multiconductor transmission lines," IEEE Trans. Microwave Theory Tech., MTT-37(1), pp. 127-138.

Palusinski, O.A., J.L. Prince, A.C. Cangellaris, B. Cooke, and L. Vakanas (1988), "Modeling and simulation of coupled, lossy lines for VLSI interconnections," Proc. of the IEEE International Conference on Computer Design, pp. 82-86.

Pozar, D.M. (1990), Microwave Engineering, Addison-Wesley, New York, pp. 319-320

Rao, S.M., T.K. Sarkar, and R.F. Harrigton (1984), "The Electrostatic Field of Electrostatic Bodies in Multiple Dielectric Media," IEEE Trans. Microwave Theory Tech., MTT-32(11), pp. 1441-1448.

Scheinfein, M.R. and O.A. Palusinski (1987), "Methods of calculation of electrical parameters for electronic packaging applications," Transactions of the Society for Computer Simulation, 4, pp. 187-254.

Telles, J.C.F. (1987), "A Self-Adaptive Co-ordinate Transformation for Efficient Numerical Evaluation of General Boundary Element Integrals," International Journal for Numerical Methods in Engineering, 24, pp. 959–973.

Tummala, R.R. and E.J. Rymaszewski (1989), hbox Microelectronic Packaging Handbook, Van Nostard Reinhold, New York.

Wait, J.R. (1985), Electromagnetic Wave Theory, Harper and Row, New York, pp. 18-21

Wei, C., R.F. Harrigton, J.R. Mautz, and T.K. Sarkar (1984), "Multiconductor Transmission Lines in Multiple Dielectric Media," IEEE Trans. Microwave Theory Tech., MTT-32(4), pp. 439-449.

Wu, R., (1988), "Interperiod Capacitance Calculations for Three-Dimensional Multiconductor Systems," IEEE Trans. Microwave Theory Tech., MTT-36(4), pp. 1515-1520.

Wu, R. and L.L. Wu (1988), "Exploiting Structure Periodicity and Symmetry in Capacitance Calculations for Three-Dimensional Multiconductor Systems," IEEE Trans. Microwave Theory Tech., MTT-36(9), pp. 1311-1318.